

1   **Leaf Bidirectional Reflectance Distribution Function (BRDF) Prediction**  
2   **with Phenotypic Traits in Four Species: Development of a Novel Measuring**  
3   **and Analyzing Framework**

4   **Liangchao Deng<sup>1,2</sup>, Leo Xinqi Yu<sup>2</sup>, Linxiong Mao<sup>2</sup>, Yanjie Wang<sup>2</sup>, Xiyue Guo<sup>3</sup>,**  
5   **Minjuan Wang<sup>3</sup>, Yali Zhang<sup>1\*</sup>, Qingfeng Song<sup>2\*</sup>, Xin-Guang Zhu<sup>2\*</sup>**

6   <sup>1</sup>The Key Laboratory of Oasis Eco-agriculture, Xinjiang Production and Construction  
7   Group, Shihezi University, Shihezi 832003, China.

8   <sup>2</sup>Key Laboratory of Plant Carbon Capture, CAS Center for Excellence in Molecular  
9   Plant Sciences, Institute of Plant Physiology and Ecology, Chinese Academy of  
10   Sciences, Shanghai 200032, China.

11   <sup>3</sup>Key Lab of Smart Agriculture Systems, Ministry of Education, College of Information  
12   and Electrical Engineering, China Agricultural University, Beijing 100083, China.

13

14   \*Address correspondence to: zhuxg@cemps.ac.cn, songqf@cemps.ac.cn,  
15   zhangyali\_cn@foxmail.com.

16   **Abstract**

17   Light intensity and spectral distribution within plant canopies provides insights into the  
18   effects of optimizing canopy architecture on light use efficiency. Breeding crop  
19   varieties with a “smart” canopy, characterized by erect upper-layer leaves and flat  
20   lower-layer leaves, can be supported with a 3D canopy model which can simulate light  
21   distribution for a particular canopy architecture. Leaf optical properties are required  
22   parameters for such canopy photosynthesis model to accurately predict canopy  
23   microclimate and hence photosynthetic efficiency. In this study, we developed a  
24   strategy to estimate the leaf optical properties based on leaf anatomical features. We  
25   developed a Directional Spectrum Detection Instrument (DSDI) system and associated  
26   Bidirectional Reflectance Distribution Function (BRDF) analysis software to precisely

27 describe leaf light distribution. BRDF parameters were quantified with high accuracy  
28 ( $R^2 > 0.95$ ) for adaxial and abaxial surfaces of maize, rice, cotton, and poplar leaves  
29 across canopy layers. Leaf phenotypic traits, surface roughness, pigments content,  
30 specific leaf weight and thickness were also assessed. Ensemble learning (EL) model  
31 showed excellent predictive performance for leaf optical properties based on  
32 phenotypic traits with  $R^2$  between 0.83 and 0.99. Compared to existing BRDF  
33 measurement systems, the DSDI achieves broader angular coverage (- $\pi/36$  to  $35\pi/36$ )  
34 via mechanical rotation design, and the ensemble learning model establishes the first  
35 direct predictive relationship between BRDF parameters and leaf phenotypic traits. This  
36 work presents a new approach to quantify leaf optical properties and offers predictive  
37 models for leaf optical properties, which can support canopy light distribution  
38 prediction and hence support design leaf features for higher canopy photosynthesis  
39 efficiency.

## 40 **Introduction**

41 Canopy photosynthesis is the sum of the photosynthesis of all aboveground tissues,  
42 which correlates with biomass accumulation and improving canopy photosynthesis is a  
43 major breeding target for crop high light use efficiency [1]. Canopy architecture  
44 primarily determines the absorption and distribution of solar light within a canopy [2]  
45 and controls the use of light energy to achieve a greater canopy photosynthetic rate [3,4].  
46 The intensity of light and spectral signals, such as red/far red ratio, regulates plant  
47 morphology, which also influences canopy photosynthesis [5]. Improving plant  
48 architecture for an optimal canopy architecture under higher planting density is widely  
49 used in crop breeding and cultivation for higher crop yield [6,7]. The rice ideotype  
50 which includes erect top leaves and medium number of tillers has been widely applied  
51 in breeding [8]. The maize “smart” canopy with small leaf angle for top leaves and large  
52 leaf angle for bottom leaves is suitable for higher planting density, which is a major  
53 contributor to maize yield in the past decades [9]. Similarly in soybean, plants with  
54 compact structures and narrower leaves are adapted for high density planting for higher

55 yield [10,11]. Plant architectural traits, including plant height and leaf angles, are also  
56 extensively optimized for other crops, such as wheat and cotton [12,13]. Though with  
57 these successes, designing and optimizing canopy architecture still represents a major  
58 target for current crop breeding. Studying genetic mechanisms underlying various plant  
59 architectural features is also a major research area in current plant biology research  
60 community.

61 By constructing a 3D canopy photosynthesis model, optimal plant architecture can  
62 be studied [14,15]. 3D canopy models can be built based on either mathematical models  
63 parameterized with plant structural parameters [16], data directly obtained from 3D  
64 plant phenomics platform, such as multi-view stereo imaging [17,18] and lidar [19,20].  
65 Accurately characterization of light distribution within a canopy is critical for designing  
66 ideal canopy architecture for higher canopy photosynthesis efficiency [21,22]. Ray  
67 tracing algorithm has been used to effectively simulate the absorbed light, transmitted  
68 light, and reflected light after light ray reaches the leaf surface [23,24]. The spatial  
69 distribution pattern of the transmitted and reflected light, which is determined by leaf  
70 optical properties, is essential for the accurate prediction of light environment inside a  
71 canopy with a ray tracing algorithm.

72 Leaves mainly absorb visible light between wavelengths 400-700 nm. The  
73 absorption coefficient is usually higher than 0.9 for blue photons and higher than 0.7  
74 for green photon. The pigment content has a major influence on the absorption  
75 coefficient. Leaves absorb less infrared light with wavelength 700-1000 nm [25,26].  
76 The spatial distribution patterns of reflected infrared light is more uniform than those  
77 for visible light [27]. Leaf surface roughness and pigment content significantly  
78 influence the distribution of reflected light [28,29]. Leaf surface roughness varies  
79 among plant species, e.g., the roughness of rice leaf is high while the roughness of  
80 cotton leaf is low. The light incident angle also affects the distribution of reflected light  
81 [30]; leaf angle similarly influences light distribution in canopy. The adaxial and abaxial  
82 surfaces have different optical properties due to the cellular anatomy of leaf section and  
83 the chlorophylls distributions inside a leaf, which differ dramatically between flat and

84 vertical leaves [31].

85 Although recent advances in 3D canopy modeling and smart breeding have  
86 highlighted the critical role of leaf optical properties in regulating canopy  
87 photosynthesis, practical evaluation of these parameters remains challenging. Existing  
88 canopy photosynthesis models often incorporate radiative transfer but typically assume  
89 uniform optical properties among leaves [32], overlooking the variability caused by  
90 environmental conditions and developmental stages, which reduces the predictive  
91 power of canopy photosynthesis models in both mechanistic studies and breeding  
92 applications. Optical instruments can directly measure leaf reflectance and  
93 transmittance [33], yet these measurements are slow and impractical for large-scale  
94 phenotyping. This limitation hampers the integration of leaf-level optical diversity into  
95 large-scale phenotyping and canopy photosynthesis modeling. In contrast, predicting  
96 optical parameters from measurable biochemical and structural traits offers a rapid  
97 alternative for characterizing leaf optical diversity and improving the parameterization  
98 of canopy photosynthesis models. Because anatomical structures and pigment  
99 compositions fundamentally determine leaf scattering and absorption [34], establishing  
100 quantitative relationships between these traits and optical parameters provides a  
101 scalable and efficient means of estimating leaf optical behavior across species and  
102 canopy positions.

103 The spatial distributions of reflected light and transmitted light, can be described  
104 with a Bidirectional Reflectance Distribution Function (BRDF), which have specific  
105 parameters including roughness ( $\sigma(\lambda)$ ), diffuse reflection coefficient ( $k(\lambda)$ ) and  
106 refractive index ( $n(\lambda)$ ) [35]. A variety of specialized equipment have been developed  
107 to sample the bidirectional and spectral reflectance of leaves and interpreted the spectral  
108 and directional variations in leaf reflectance with BRDF [36,37]. Among these  
109 parameters,  $\sigma(\lambda)$  is primarily affected by epidermal micromorphology and surface  
110 irregularities [38];  $k(\lambda)$  depends on mesophyll scattering related to leaf thickness and  
111 internal spaces [39]; and  $n(\lambda)$  is influenced by biochemical composition [40].  
112 Therefore, BRDF parameters are inherently linked to leaf anatomy, pigment

113 composition, and physiological traits. Predicting BRDF parameters from leaf anatomy  
114 and physiological traits can be a potential efficient method. However, the quantitative  
115 relationships between BRDF parameters and these leaf traits remain poorly understood,  
116 and no predictive model currently exists for estimating BRDF parameters directly from  
117 leaf anatomical and physiological data.

118 To bridge this gap, we propose a scalable, phenomics-oriented approach to quantify  
119 leaf optical properties from measurable anatomical and biochemical traits. We  
120 developed a Directional Spectrum Detection Instrument (DSDI) that allows efficient  
121 measurement of leaf Bidirectional Reflectance Distribution Function (BRDF) across a  
122 broad range of illumination and viewing angles. The BRDF model was parameterized  
123 using roughness ( $\sigma(\lambda)$ ), diffuse reflection coefficient ( $k(\lambda)$ ), and refractive index  
124 ( $n(\lambda)$ ), which link physical surface scattering and internal absorption processes to  
125 measurable leaf traits. Moreover, we established an ensemble learning (EL) framework  
126 to predict BRDF parameters based on leaf phenotypic traits such as thickness, specific  
127 leaf weight, pigment content, and surface roughness. This integration of optical  
128 measurement, modeling, and data-driven prediction establishes a new pathway toward  
129 computational phenotyping of optical traits, facilitating the parameterization of 3D  
130 canopy models for photosynthesis simulation.

131 Table 1. Description of symbols used in the paper.

Symbol	Quantity	Unit (symbol)
$L$	Illumination direction vector	None
$V$	Viewing direction vector	None
$N$	Normal to the sample vector	None
$H$	Diagonal vector of $L$ and $V$	None
$\lambda$	Wavelength	Nanometer (nm)
$\theta$	Zenith angle	Degree (°)
$\phi$	Azimuth angle	Degree (°)
$\alpha$	Angle between $N$ and $H$	Degree (°)
$\theta_h$	Half of the phase angle between $L$ and	Degree (°)

---

*V*

$f_{brdf}$	Bidirectional reflectance	Unit per steradian ( $sr^{-1}$ )
$f_{samp}$	Bidirectional reflectance of sample	Unit per steradian ( $sr^{-1}$ )
$f_{ref}$	Bidirectional reflectance of reference	Unit per steradian ( $sr^{-1}$ )
$f_{spec}$	Reflectance of specular component	Unit per steradian ( $sr^{-1}$ )
$f_{diff}$	Reflectance of diffuse component	Unit per steradian ( $sr^{-1}$ )
$dA$	Unit area	Square meter ( $m^2$ )
$d\Omega$	Unit solid angle	Steradian ( $sr$ )
$\phi$	Radiant flux	Watt ( $W$ )
$L_r$	Radiance	Watt per square meter per steradian ( $W \cdot m^{-2} \cdot sr^{-1}$ )
$E$	Irradiance	Watt per square meter ( $W \cdot m^{-2}$ )
$\sigma(\lambda)$	Roughness	None
$k(\lambda)$	Diffuse reflection coefficient	None
$n(\lambda)$	Refractive index	None
$Chl.\,a$	Content of leaf chlorophyll a	( $mg \cdot dm^{-2}$ )
$Chl.\,b$	Content of leaf chlorophyll b	( $mg \cdot dm^{-2}$ )
$Chl.\,a + b$	Total chlorophyll content (sum of $Chl.\,a$ and $Chl.\,b$ )	( $mg \cdot dm^{-2}$ )
$Car.$	Leaf carotenoid content	( $mg \cdot dm^{-2}$ )
$T$	Leaf thickness	(mm)
$SLW$	Specific leaf weight	( $g \cdot m^{-2}$ )
$\rho$	Leaf roughness measured by section	None

---

132 subscripts  $\lambda$ ,  $i$  and  $v$  represent the wavelength, illumination and viewing directions.

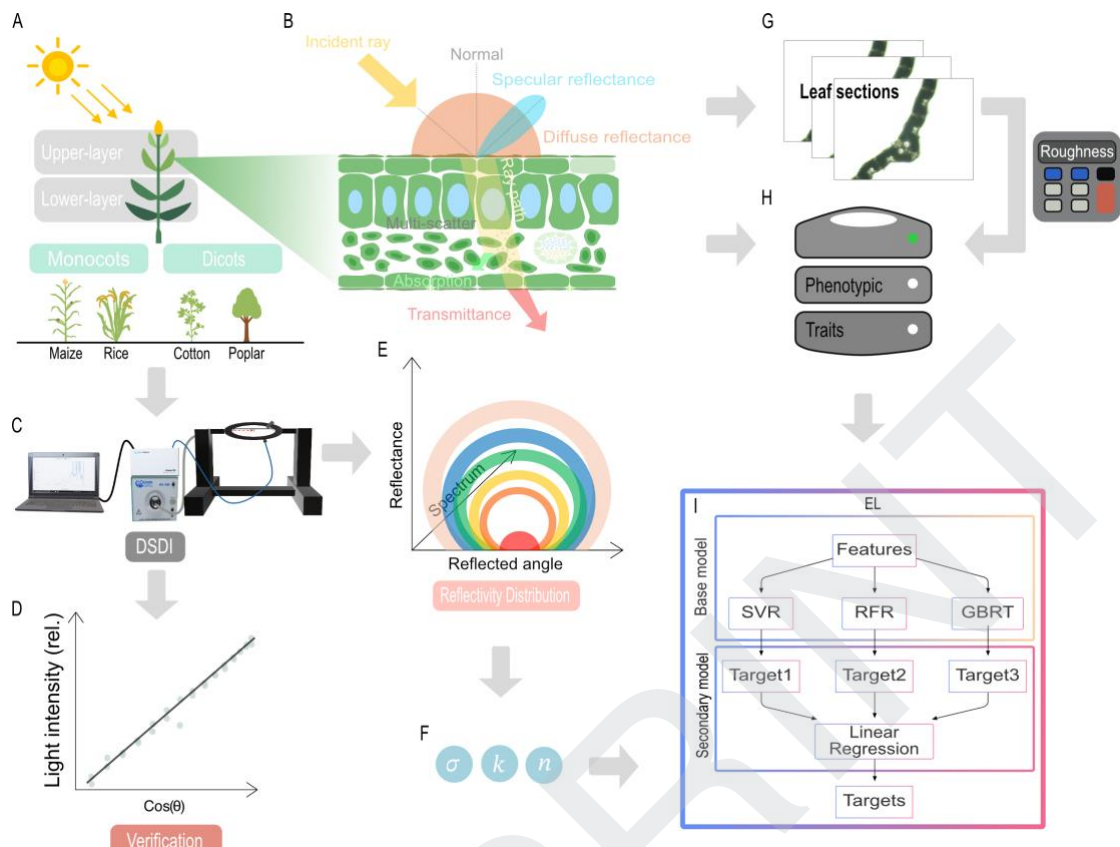
133 **Materials and Methods**

134 **Experimental Design**

135 This study investigated the relationships between leaf phenotypic traits and  
136 Bidirectional Reflectance Distribution Function (BRDF) parameters for leaves from  
137 different plant species and from different canopy layers with a goal of developing a

138 predictive framework for leaf optical properties. As shown in **Fig. 1**, four plant species  
139 including maize (*Zea mays* L.), rice (*Oryza sativa* L.), cotton (*Gossypium hirsutum* L.)  
140 and poplar (*Populus alba* L.) were used in this study. The adaxial and abaxial surfaces  
141 of these leaves from both upper and lower layer of canopies were measured.  
142 Reflectance light distribution was measured with a custom-built Directional Spectrum  
143 Detection Instrument (DSDI), calibrated using a **diffuse whiteboard standard (WS-1,**  
144 **PTFE-based Lambertian material; Ocean Insight Inc., USA)** with reflectivity greater  
145 than **98% across 250–1500 nm.** Leaf optical property related traits, including  
146 chlorophyll a(*Chl. a*), chlorophyll b (*Chl. b*), carotenoid content (*Car.*), specific leaf  
147 weight (SLW), and thickness (T), were quantified with established protocols. Leaf  
148 surface roughness was determined using a custom developed image processing  
149 software, Roughness Calculator (RC), based on the leaf section microscopy images.

150 To analyze the effects of species and canopy layer on leaf phenotypic traits, two-  
151 way ANOVA was **conducted using R software (version 4.5.1; R Core Team, 2023).** The  
152 analysis was implemented with the *car* package for Type III sum-of-squares ANOVA  
153 [41], and post-hoc multiple comparisons were performed using the *emmeans* [42] and  
154 *rstatix* packages [43]. Independent *t*-test for group comparison was conducted in Excel  
155 (Microsoft Corporation, Redmond, WA, USA, version 365). BRDF parameter fitting  
156 was performed in MATLAB (MathWorks Inc., Natick, MA, USA, version 2024b),  
157 ensuring a high precision in parameter estimation. Furthermore, an ensemble learning  
158 model was developed in Python (version 3.8; Python Software Foundation) with a  
159 *scikit-learn* library [44]. Model performance was assessed through cross-validation and  
160 evaluated using metrics including coefficient of determination ( $R^2$ ) and mean square  
161 error (*MSE*) to validate predictive accuracy.



162

163 **Figure 1.** Schematic of the experimental design and the development of the predictive framework for  
164 optical properties. The upper- and lower-layer leaves from four plant species (maize, rice, cotton, and  
165 poplar), categorized into monocots and dicots, were used (A). Light was absorbed by a leaf and reflected  
166 and transmitted from the leaf. The reflect light includes specular and diffuse portion, and this reflect light  
167 distribution can be modeled with BRDF (B). Leaf section microscopy images were analyzed to obtain  
168 surface roughness data (G), which, along with other phenotypic traits (H), were fed into a predictive  
169 model. The DSDI platform was developed for measuring leaf reflect light distribution (C), calibrated for  
170 data accuracy with white board standard (D). Data of anatomical and physiological traits and the reflect  
171 light distribution data were used to develop ensemble learning (EL) model, including Support Vector  
172 Regression (SVR), Random Forest Regression (RFR), and Gradient Boosting Regression Tree (GBRT),  
173 for accurate prediction of BRDF parameters, roughness ( $\sigma(\lambda)$ ), diffuse reflection coefficient ( $k(\lambda)$ ) and  
174 refractive index ( $n(\lambda)$ ). This study develops the BRDF parameter acquisition tools and its prediction  
175 model based on the data of leaf anatomical and physiological traits, which supports canopy light-use  
176 efficiency modeling.

## 177 Plant Materials

178 The experiment was conducted in 2021 at the Institute of Plant Physiology and Ecology,  
179 Chinese Academy of Sciences (CAS), Shanghai, China. Four plant species were used  
180 in this study including maize, rice, cotton and poplar. All plants were grown in a  
181 greenhouse with controlled environment, day/night temperatures of 25/18°C and a  
182 relative humidity of 60-70%. At the time of measurement, maize plants were

183 approximately 2.0 m tall at the silking stage, rice plants at the heading stage were about  
184 0.9 m tall, cotton plants at the boll-forming stage were about 1.5 m tall, and poplar  
185 plants were about 2.0 m tall at the vigorous growth stage. To capture the variability in  
186 optical properties across canopy layers, leaves were sampled from both upper and lower  
187 canopy positions, defined as the upper and lower halves of the plant height, respectively.  
188 For each species, at least 3 plants were used and at least 6 leaves from each plant were  
189 used for the measurements, with fully expanded leaves sampled from both upper and  
190 lower layers in canopy. For each leaf, both adaxial and abaxial surfaces were measured  
191 separately.

### 192 **Ray tracing simulations for evaluation of canopy scatter light distribution**

193 To quantify the effect of BRDF parameters on the spatial distribution of scattered light  
194 within plant canopies, ray tracing simulations were performed using a 3D rice canopy  
195 model (cultivar 9311 at the heading stage). The simulations were conducted with an  
196 optimized version based on the original ray tracing software (fastTracer, published by  
197 Song et al, 2013) [45]. The optimized version of fastTracer is available at  
198 <https://github.com/PlantSystemsBiology/fastTracerPublic>), which was further  
199 modified for this study to incorporate variable BRDF parameters. The 3D canopy model  
200 consisted of triangular leaf facets reconstructed from morphological measurements,  
201 representing the realistic spatial architecture of rice plants. Each photon was tracked  
202 through interactions with leaf surfaces, including reflection, transmit, and absorption,  
203 which were governed by the Cook–Torrance BRDF model.

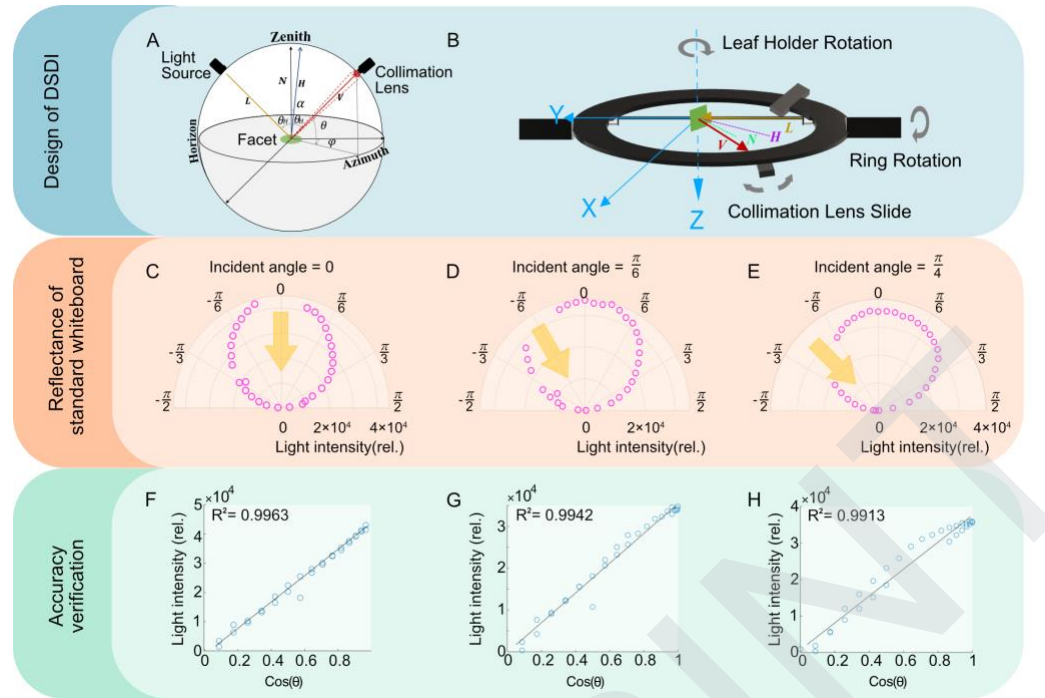
204 To evaluate the individual and combined effects of the BRDF parameters,  
205 simulations were conducted under different combinations of leaf roughness ( $\sigma$ ), diffuse  
206 reflection coefficient ( $k$ ), and refractive index ( $n$ ). The tested parameter sets included  
207  $(\sigma, k, n) = (0.3, 0.01, 1.0), (0.3, 0.35, 1.0), (1.0, 0.01, 1.0), (0.3, 0.01, 2.2), (1, 0.35,$   
208  $2.2)$  and  $(0.3, 0.35, 2.2)$ . For each configuration, photons were emitted from the light  
209 source and traced until absorption or exit from the canopy domain. The resulting  
210 scattered photosynthetic photon flux density (PPFD) values were recorded at different  
211 canopy heights. The canopy space was divided into multiple horizontal layers of equal

212 thickness, and the averaged PPFD were computed for each layer.

## 213 Development and evaluation of the DSDI system

214 The custom-built Directional Spectrum Detection Instrument (DSDI) is used to capture  
215 the angular spectrum from leaf surfaces (Fig. 1C). The DSDI setup incorporates an  
216 HPX-2000 high-power xenon light source (Detailed in **Table S1**) and an HR2000 high-  
217 resolution fiber optic spectrometer (Detailed in **Table S2**) (Ocean Insight Inc., USA).  
218 The distribution of reflectance on a leaf surface is typically characterized by the angular  
219 distribution of zenith ( $\theta$ ), and azimuth ( $\varphi$ ) angles in spherical coordinates,  
220 visualized as the reflection hemisphere [46]. **Figure 2A** illustrates the geometric  
221 relationship between incident and reflection angles, with the upper hemisphere  
222 representing the reflecting hemisphere. The measurement platform in DSDI has three  
223 axes (**Fig. 2B**), first, the leaf holder can be rotated with the Z-axis determining the  
224 illumination angle ( $\theta_i, \varphi_i$ ); second, the detection ring can be rotated with the Y-axis  
225 and third, the collimation lens can be slide on the detection ring. The detection ring and  
226 the collimation lens together determines the detecting angle ( $\theta_v, \varphi_v$ ). When leaf  
227 sample was placed into a leaf holder, the collimation lens then rotated around the leaf  
228 holder on a circular track, capturing measurements from multiple angles. For detailed  
229 information, see supplementary material (**Fig. S1-S3**).

230 To validate the accuracy of DSDI in the measurement of reflectance from different  
231 angles, we conducted tests using a Lambertian whiteboard with its reflectance  
232 following the Lambert cosine law, i.e., the reflect light intensity is linearly correlated  
233 with the cosine of the detection angle [47,48]. Reflect light intensity at different  
234 detection angles was measured and recorded for the whiteboard at incidence angles of  
235 0,  $\pi/6$  and  $\pi/4$ , respectively. (**Fig. 2C-E**). A linear relationship was derived between  
236 reflectance intensity and cosine of the detection angle ( $R^2 > 0.99$ ) (**Fig. 2F-H**),  
237 confirming that DSDI provides reliable spatial light distribution measurements.



238

239 Figure 2. The design and verification of DSDI. A: the geometric design of the optical platform in DSDI,  
 240 including rotating the leaf holder determining the illumination angle ( $\theta_i, \varphi_i$ ), rotating detection ring and  
 241 sliding collimation lens determining the viewing or detecting angle ( $\theta_v, \varphi_v$ ). B: the measurement  
 242 diagram of DSDI. C-E: data of reflectance intensity measured with a standard whiteboard at incidence  
 243 angles of 0,  $\pi/6$  and  $\pi/4$ , and plotted in a polar coordinate system. Yellow arrows indicate the incident  
 244 light direction. F-H: the linear relationship between reflectance intensity and  $\cos(\theta)$  at the three  
 245 corresponding incidence angles (0,  $\pi/6$  and  $\pi/4$ ).  $\theta$  represents the angle between the viewing  
 246 direction and the normal.

## 247 Measurement of spatial distribution of reflection spectrum of leaves

248 The directional distribution of transmitted light through leaves is physically similar to  
 249 that of diffuse reflectance [33], and it can be approximated by a Lambertian function  
 250 [49]. Therefore, this study focuses on the reflection distribution without separately  
 251 analyzing the transmission component. The DSDI system was used to measure the  
 252 reflection distribution of leaf as the following steps. Firstly, a leaf sample with area of  
 253  $1\text{cm} \times 2\text{ cm}$  was attached on the leaf holder. The leaf surface should be flat, and the  
 254 position of the primary vein was not used. Secondly, the sample holder was rotated to  
 255 set the incident angle. The light source was turned on, and a light spot can be observed  
 256 on the leaf. The illuminated area is round for incident angle 0 and elliptical for other  
 257 incident angles. Thirdly, the detection ring was rotated to be horizontal for measuring  
 258 the reflection and then the collimation lens was slide along the detection ring to measure

259 the reflect light spectrum at different reflection angles. Finally, the reflected light  
260 spectrum was measured and recorded by the spectrometer and the PC.

261 We collected reflectance data across a broad spectrum (400 – 992 nm) and selected  
262 five representative wavelengths (468.36, 556.26, 673.46, 819.88, and 877.97nm) for  
263 further analysis as shown in **Table 2**. These wavelengths include the primary absorption  
264 (468.36 and 673.46 nm) for pigments such as *Chl. a*, *Chl. b*, and *Car*; the maximum  
265 reflectance peak in the green light region (556.26 nm); the near-infrared (NIR) region  
266 (819.88 and 877.97 nm).

267 Table 2. The selected wavelengths in the VIS-NIR spectrum.

	Waveband	Blue	Green	Red	Near-infrared
269	Range(nm)	440-485	500-565	625-740	800-1300
271	Wavelength(nm)	468.36	556.26	673.46	819.88, 877.97

272 **The definition of BRDF and its calculation based on the measured data with DSDI  
273 system**

274 The Bidirectional Reflectance Distribution Function (BRDF) is used to describe the  
275 spatial reflecting characteristics of light on rough surfaces, such as the leaf surface [50].  
276 The general bidirectional reflectance ( $f_{brdf}$ ) can be defined as the ratio of radiance to  
277 irradiance, quantifying the contribution of the incident spectral irradiance from the  
278 direction  $(\theta_i, \varphi_i)$  to the reflected spectral radiance in the direction  $(\theta_v, \varphi_v)$  (**Eq. 1**).  
279 Radiance is the radiant flux (power) per unit projected area per unit solid angle (unit:  
280  $\text{W}\cdot\text{sr}^{-1}\cdot\text{m}^{-2}$ ) and irradiance is the radiant flux incident on a surface per unit surface area.

281 
$$f_{brdf} = \frac{L_r(\lambda, \theta_i, \varphi_i, \theta_v, \varphi_v)}{E(\lambda, \theta_i, \varphi_i)} \quad (1)$$

282 The  $f_{brdf}$  represents the bidirectional reflectance,  $L$  denotes radiance,  $E$  refers to  
283 irradiance,  $\lambda$  is the wavelength,  $\theta_i$  is incident zenith angle, and  $\varphi_i$  is the incident  
284 azimuth angle,  $\theta_v$  is reflex zenith angle, and  $\varphi_v$  is the reflex azimuth angle. The  
285 symbols and units used in this formula are summarized in **Table 1**.

286 According to the definitions, the radiance ( $L_r$ ) can be derived with the measured

287 reflected radiant flux ( $\phi_v$ ) at a view angle ( $\theta_v$ ) for a certain surface area ( $dA$ ) and a  
 288 certain solid angle ( $d\Omega$ ) as **Eq. 2**.

$$289 \quad L_{\text{v}} = \frac{\phi_v}{dA \cos(\theta_v) d\Omega} \quad (2)$$

290 The irradiance ( $E$ ) can be derived with the incident radiant flux ( $\phi_i$ ) on the surface  
 291 area ( $dA$ ) with **Eq. 3**.

$$292 \quad E = \frac{\phi_i}{dA} \quad (3)$$

293 Substituting **Eq. 2** and **Eq. 3** into the **Eq. 1**, we obtain **Eq. 4** that describes the  
 294 bidirectional reflectance for light at wavelength ( $\lambda$ ) with incident direction ( $\theta_i, \varphi_i$ )  
 295 and reflect direction ( $\theta_v, \varphi_v$ ):

$$296 \quad f_{\text{braf}}(\lambda, \theta_i, \varphi_i, \theta_v, \varphi_v) = \frac{L(\lambda, \theta_i, \varphi_i, \theta_v, \varphi_v)}{E(\lambda, \theta_i, \varphi_i)} = \frac{\phi_v}{\phi_i \cos(\theta_v) d\Omega} \quad (4)$$

297 Assuming that the reference whiteboard behaves as an ideal Lambertian surface  
 298 with a hemispherical reflectance of 100%, the bidirectional reflectance of the reference  
 299 surface is  $1/\pi$  [51]:

$$300 \quad f_{\text{ref}} = \frac{\phi_{v,\text{ref}}}{\phi_i \cos(\theta_v) d\Omega} = \frac{1}{\pi} \quad (5)$$

301 Thus, the bidirectional spectral reflectance of the leaf sample can be calculated  
 302 relative to the whiteboard as following equations:

$$303 \quad f_{\text{samp}} = \frac{\phi_{v,\text{samp}}}{\phi_i \cos(\theta_v) d\Omega} = \frac{\phi_{v,\text{samp}}}{\pi \cdot \phi_{v,\text{ref}}} \quad (6)$$

304 Using the DSDI system, the measurement was performed for leaves and the  
 305 reference whiteboard at several incident angles. For each incident angle ( $i$ ), the  
 306  $\phi_{v,\text{samp}}$  and  $\phi_{v,\text{ref}}$  at various reflection angles were measured. Then the bidirectional  
 307 reflectance for leaf sample ( $f_{\text{samp}}$ ) could be calculated with **Eq. 6**.

308 In the practical operation of the DSDI system, all angular parameters are derived  
 309 from the instrument's mechanical scales. Due to minor manufacturing and assembly  
 310 deviations, the initial position of the leaf holder does not correspond to a true  $0^\circ$   
 311 orientation but instead to  $95^\circ$ , which represents the perpendicular illumination reference

312 of the DSDI. Therefore, the leaf inclination angle  $\theta_{leaf}$  was calculated with the scale  
 313 of leaf holder ( $\theta_{leafholder}$ ) as:

$$314 \quad \theta_{leaf} = 95^\circ - \theta_{leafholder} \quad (7)$$

315 where  $95^\circ$  corresponds to the perpendicular illumination reference of the DSDI system.

316 To facilitate the calculation of reflection geometry, a three-dimensional Cartesian  
 317 coordinate system was established (Fig. 2B). The illumination direction was defined as  
 318 the positive direction of the Y-axis, while the Z-axis points vertically downward. The  
 319 X-axis was defined according to the right-handed Cartesian coordinate system,  
 320 perpendicular to the YZ-plane. Since the light source remained fixed, the illumination  
 321 direction vector ( $L$ ) was defined as:

$$322 \quad L = (0, -1, 0) \quad (8)$$

323 Based on the leaf inclination angle, the leaf normal vector ( $N$ ) can be expressed as:

$$324 \quad N = (\sin(\theta_{leaf}), -\cos(\theta_{leaf}), 0) \quad (9)$$

325 During reflection measurements, the collimation lens slides along the detection  
 326 ring to acquire reflectance at different angles. The ring's scale reading corresponds to  
 327 the viewing zenith angle ( $\theta_v$ ), while the rotation of the ring defines the viewing azimuth  
 328 angle ( $\varphi_v$ ). Accordingly, the viewing direction vector ( $V$ ) can be calculated as:

$$329 \quad V = (\sin(\theta_v) \cos(\varphi_v), -\sin(\theta_v), \sin(\theta_v) \sin(\varphi_v)) \quad (10)$$

330 Based on the illumination direction vector ( $L$ ) and the viewing direction vector ( $V$ ),  
 331 the half-vector ( $H$ ) representing the bisector of illumination and viewing directions is  
 332 calculated as:

$$333 \quad H = \frac{L + V}{\sqrt{(L + V, L + V)}} \quad (11)$$

334 Thus, all directional vectors and angular parameters required for the BRDF model,  
 335 including the illumination, viewing, normal and half vectors, were determined  
 336 geometrically within this coordinate framework.

### 337 The Cook-Torrance model for BRDF

338 In this study, we employ the classic Cook-Torrance model to calculate BRDF. The

339 model was developed by Robert Cook and Kenneth Torrance in 1981 for surface with  
 340 varying roughness based on geometric optics [52]. The reflectance of a rough surface  
 341 lies between perfect diffuse and perfect specular reflectance, and can be expressed as  
 342 the sum of the diffuse and specular components:

$$343 \quad f_{brdf} = f_{spec} + f_{diff} \quad (12)$$

344 For an ideal Lambertian surface, the bidirectional reflectance is  $1/\pi$  [51]. The  
 345 diffuse component of the bidirectional reflectance for a leaf surface can be expressed  
 346 as [Eq. 12](#) and the  $k(\lambda)$  is the diffuse reflection coefficient.

$$347 \quad f_{diff} = \frac{k(\lambda)}{\pi} \quad (13)$$

348 The specular reflection component is more complex than the diffuse reflection. The  
 349 leaf surface can be approximated as a collection of micro-facets with irregular  
 350 orientations [53], as shown in [Fig. 1B](#). Specular reflection in this model is described as  
 351 light reflecting from micro-facets, with the reflection occurring between the  
 352 illumination and the viewing.

353 The leaf cuticle, which covers the epidermal cells, is considered a low-absorption  
 354 medium compared to the leaf itself [54], allowing us to neglect its absorption. The light  
 355 reflected from a single micro-facet can be defined by the Fresnel factor  $F(n, \theta)$ , which  
 356 describes the proportion of non-polarized incident light reflected as specular reflection  
 357 [55]:

$$358 \quad F(n, \theta_h) = \frac{1}{2} \left( \frac{n^2(\lambda) + \cos^2(\theta_h) - 1 - \cos(\theta_h)}{n^2(\lambda) + \cos^2(\theta_h) - 1 + \cos(\theta_h)} \right)^2 \left[ 1 + \left( \frac{\cos(\theta_h) (n^2(\lambda) + \cos^2(\theta_h) - 1 + \cos(\theta_h)) - 1}{\cos(\theta_h) (n^2(\lambda) + \cos^2(\theta_h) - 1 - \cos(\theta_h)) + 1} \right)^2 \right] \quad (14)$$

359 The distribution of the micro-facet slopes is defined by the Beckmann distribution  
 360  $D(\alpha, \sigma)$ , which can be expressed as [56]:

$$361 \quad D(\alpha, \sigma) = \frac{e^{-\left(\frac{\tan(\alpha)}{\sigma}\right)^2}}{\sigma^2 \cos^4(\alpha)} \quad (15)$$

362 During illumination, micro-facets may shield and mask each other, causing light  
 363 attenuation [37]. The geometric attenuation factor  $G(\mathbf{L}, \mathbf{N}, \mathbf{V}, \mathbf{H})$  describes this effect,  
 364 capturing the reduction of light due to multiple reflections between micro-facets [57]:

365

$$G(\mathbf{L}, \mathbf{N}, \mathbf{V}, \mathbf{H}) = \min \left( 1, \frac{2(\mathbf{V}, \mathbf{N})(\mathbf{N}, \mathbf{H})}{(\mathbf{V}, \mathbf{H})}, \frac{2(\mathbf{L}, \mathbf{N})(\mathbf{N}, \mathbf{H})}{(\mathbf{V}, \mathbf{H})} \right) \quad (16)$$

366 Here,  $\mathbf{H}$  is the angular bisector vector and can be calculated with Eq. 11 by  
 367 assuming that  $\mathbf{H}$  is the normal vector of the micro-facet [36].

368 In summary, the Cook-Torrance BRDF on the leaf surface can be expressed as:

369

$$f_{brdf} = \frac{F(n(\lambda), \theta_h) \cdot D(\alpha, \sigma(\lambda)) \cdot G(\mathbf{L}, \mathbf{N}, \mathbf{V}, \mathbf{H})}{2\pi^2(\mathbf{L}, \mathbf{N})(\mathbf{N}, \mathbf{V})} + \frac{k(\lambda)}{\pi} \quad (17)$$

370 **BRDF Parameters Fitting Algorithms**

371 According to the Cook-Torrance model of BRDF, three critical parameters (roughness  
 372 ( $\sigma(\lambda)$ )), diffuse reflection coefficient ( $k(\lambda)$ )), and refractive index ( $n(\lambda)$ )) of the BRDF  
 373 determines leaf optical properties. These parameters influence reflectance distribution,  
 374 which is vital for understanding light behavior on a leaf surfaces. The optimization of  
 375 BRDF parameters was constrained by setting fixed upper and lower bounds for each  
 376 parameter during the fitting process [36]. These bounds ensured that the parameter  
 377 values remained within physically meaningful and biologically relevant ranges, thereby  
 378 improving the robustness and accuracy of the optimization. The roughness,  $\sigma(\lambda)$ ,  
 379 describes the surface texture and corresponds to the root mean square (RMS) of the  
 380 slope of the micro-facets on the surface [49]. It ranges from 0 (perfectly smooth) to 1  
 381 (highly rough). A higher  $\sigma(\lambda)$  value indicates more irregular and scattered reflected  
 382 light, while a lower value results in more directional and concentrated reflections [58].  
 383 The diffuse reflection coefficient,  $k(\lambda)$ , represents the proportion of diffuse light  
 384 reflected from the surface, with values between 0 and 1. The  $k(\lambda)$  value of 0 indicates  
 385 no diffuse reflection, while a value of 1 suggests complete diffuse reflectance. The  
 386 refractive index,  $n(\lambda)$ , quantifies the extent to which light attenuates when passing  
 387 through the leaf medium and typically ranges from 1 to 5 for leaves [59].

388 To accurately characterize the BRDF parameters of leaf surfaces, we employed two  
 389 fitting methods: Least Squares curve fitting and Adaptive Grid Search. The least squares  
 390 method is a traditional regression technique that estimates parameter values by  
 391 minimizing the sum of squared residuals between observed and fitted values. Using  
 392 MATLAB's least squares fitting function, we estimated the BRDF parameters. This

method is computationally efficient and suitable for samples with relatively simple surface structures. An adaptive grid search algorithm was developed in this study, and this algorithm utilized a 2-layered grid (step sizes of  $1 \times 10^{-2}$  and  $1 \times 10^{-4}$  respectively) structure to incrementally optimize each parameter, providing a more precise approximation of true values. By iteratively narrowing the search range and increasing resolution, this method gradually converges on the optimal solution. The source code of Python for adaptive grid search algorithm was available at <https://github.com/PlantSystemsBiology/brdf>.

The solver was applied with initial values  $(\rho_0, k_0, n_0) = (0.5, 0.5, 3)$  and parameter bounds  $\rho \in [0, 1]$ ,  $k \in [0, 1]$ ,  $n \in [1, 5]$  (implemented as [0.01, 0.01, 1.1]–[0.99, 0.99, 5] for numerical stability). Model performance was evaluated by coefficient of determination ( $R^2$ ), root mean square error (RMSE) and residual analysis, providing reliable estimations of BRDF parameters for each wavelength and leaf sample.

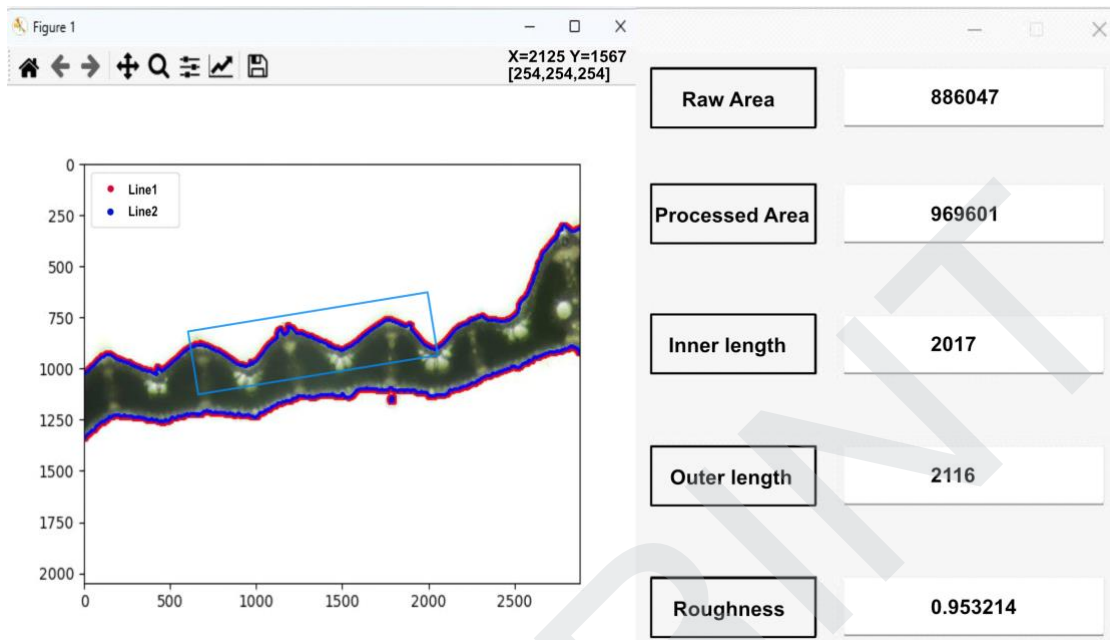
#### Quantification of Leaf Roughness Using RC

Leaf cross-sections were prepared by manually cutting 50–80  $\mu m$  segments of fresh leaves with a sharp blade [60], and images of the leaf sections were obtained using an optical microscope (Leica DM2500, Leica Microsystems, Wetzlar, Germany). A custom software tool, Roughness Calculator (RC), was developed to quantify leaf roughness (software available at <https://github.com/PlantSystemsBiology/brdf>). RC software calculated leaf roughness with the image of leaf cross-section. A region of interest (ROI) of leaf surface was selected from the leaf cross-section image (shown by the blue box) and the exact inner edge length  $l_{inner}$  (blue line) based on individual pixel counts was calculated. Then, the smoothed outer edge length  $l_{outer}$  (red line) was determined using a Gaussian filter (shown in Fig. 3). The ratio  $\rho$ , calculated with Eq. 18, provides a reliable metric for leaf surface roughness. To mitigate the effects of leaf tips and main veins, ROI can be manually selected instead of the whole section within the software. The ROI size was randomized, and five replicates were analyzed for each section image, to minimize user bias. For detailed methodology, see

422 supplementary material (**Fig. S4-S8**).

423

$$\rho = \frac{l_{inner}}{l_{outer}} \quad (18)$$



424  
425 Figure 3. Quantification of leaf surface roughness using the Roughness Calculator (RC) software. The  
426 software calculated two edge lengths of the leaf section: the precise inner edge length ( $l_{inner}$ , blue line)  
427 based on individual pixel counts and the smoothed outer edge length ( $l_{outer}$ , red line) based on a Gaussian  
428 smoothing filter. Their ratio ( $\rho = l_{inner}/l_{outer}$ ) represented the roughness metric (data were shown at the right  
429 side of the software). Manual selection of the region of interest (ROI) (light blue box) allowed analysis  
430 for a specific part of leaf surface.

### 431 Measurement of Physiological and Biochemical Traits

432 Leaf thickness (T) was measured using a micrometer. Small leaf discs were punched  
433 from the leaves avoiding the primary veins for determining the content of chlorophyll  
434 a (*Chl. a*), chlorophyll b (*Chl. b*) and carotenoid (*Car.*), following an established  
435 protocol [61]. Absorbance (A) values were measured at wavelengths of 663 nm, 645  
436 nm and 470 nm in a spectrophotometer. The calculation formulas for these pigments  
437 were as follows:

438  $Chl. a = 12.72A_{663} - 2.59A_{645} \quad (19)$

439  $Chl. b = 22.88A_{645} - 4.67A_{663} \quad (20)$

440  $Car. = \frac{1000A_{470} - 3.27C_{chl.a} - 104C_{chl.b}}{229} \quad (21)$

441 For measuring specific leaf weight (SLW), leaf samples with an area of ~6 cm<sup>2</sup>  
442 were collected. The areas of the leaf samples were first precisely measured and then the

443 leaf samples were dried at 105°C for 10 minutes and 80°C until a constant weight. The  
444 specific leaf weight (SLW) was calculated by dividing the dry weight of the leaf sample  
445 by the area:

$$446 \quad SLW = \frac{dry\ weight}{area} \quad (22)$$

447 **Development of an Ensemble Learning Model for Predicting Leaf Optical**  
448 **Properties Based on Phenotypic Traits**

449 In this study, we developed an ensemble learning (EL) model to predict the BRDF  
450 parameters of leaves with their phenotypic traits utilizing data from 270 **data entries**.  
451 The EL model integrates Support Vector Regression (SVR), Random Forest Regression  
452 (RFR), and Gradient Boosting Regression Tree (GBRT) as base learners, with a  
453 stacking strategy using Linear Regression (LR) as the meta-learner **(as shown in Fig.**  
454 **II).**

455 Nine phenotypic traits were used as input variables, including leaf thickness (T),  
456 specific leaf weight (SLW), chlorophyll a (*Chl.a*), chlorophyll b (*Chl.b*), and  
457 carotenoid content (*Car.*) total chlorophyll (*Chl.a+b*), chlorophyll *a/b* ratio  
458 (*(Chl.a)/(Chl.b)*), leaf surface roughness ( $\rho$ ), and spectral wavelength ( $\lambda$ ). These  
459 traits collectively describe the biochemical, physiological, and structural characteristics  
460 that determine leaf optical behavior and thus the BRDF parameters.

461 This EL framework was designed to improve predictive accuracy and  
462 generalization by leveraging the complementary strengths of multiple regression  
463 algorithms. The methodology involved several key steps:

464 (1) Data Preprocessing and Standardization

465 The features were standardized using z-score normalization. For each feature, the mean  
466 and standard deviation were calculated, then each sample's feature value was  
467 transformed by subtracting the mean and dividing by the standard deviation. This  
468 process resulted in a distribution with zero mean and unit variance for all features,  
469 eliminating differences in units and scales among features for enhancing model  
470 convergence and predictive performance.

471        (2) Feature Selection

472        We applied Recursive Feature Elimination (RFE) for feature selection. The RFE  
473        iteratively built models and eliminated the least significant features based on feature  
474        importance (e.g., model coefficients or feature importance scores). Using this method,  
475        five features were selected from the initial set of nine phenotypic traits according to the  
476        impact on the BRDF parameters. These five features served as independent variables  
477        for model training. The three BRDF parameters were set as target variables, and  
478        separate models were developed for each BRDF parameter.

479        (3) Model Development and Hyperparameter Optimization

480        The dataset was split into training and testing sets at an 8:2 ratio to ensure robust model  
481        training and evaluation. Using the five selected features, we developed three base  
482        models: Support Vector Regression (SVR), Random Forest Regression (RFR), and  
483        Gradient Boosting Regression (GBRT). For each base model, hyperparameter  
484        optimization was performed using 10-fold cross-validation combined with a grid search.  
485        By exhaustively testing predefined parameter combinations, a set of parameters that  
486        minimized the cross-validation mean squared error (MSE) for each model were  
487        identified.

488        (4) Ensemble Model Construction

489        We then constructed an ensemble learning (EL) model using a stacking approach. The  
490        optimized SVR, RFR, and GBRT models served as primary learners, and Linear  
491        Regression (LR) was employed as the secondary learner (meta-learner). This stacking  
492        approach allowed the EL model to combine predictions from the primary learners,  
493        enhancing the model's overall generalization capability. The performance of the EL  
494        model was further evaluated using 10-fold cross-validation.

495        (5) Model Performance Evaluation

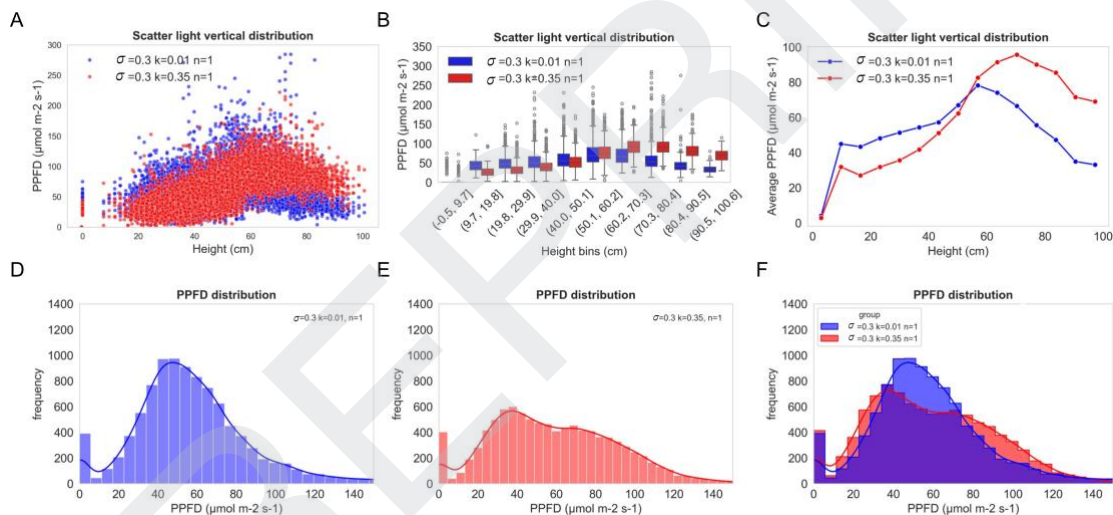
496        Finally, we evaluated the predictive performance of all models on the test set to verify  
497        their generalization abilities and practical applicability. We used Mean Squared Error  
498        (MSE) and the coefficient of determination ( $R^2$ ) as evaluation metrics to compare the  
499        base models and the EL model. This allowed us to assess and compare the accuracy and

500 reliability of each model in predicting the BRDF parameters based on leaf phenotypic  
 501 traits.

## 502 Results

### 503 Ray-tracing Analysis of BRDF Effects on Canopy Scattering

504 To quantify the impact of BRDF parameters on canopy light environments, we  
 505 incorporated the BRDF parameters in the ray-tracing software previously developed by  
 506 Song et al [60] and performed ray tracing simulations using a 3D rice canopy model.  
 507 The canopy light simulation focused on the distribution of leaf-scattered photosynthetic  
 508 photon flux density (PPFD), as BRDF parameters mainly regulate the scattering  
 509 behavior of leaf surfaces rather than atmospheric direct or diffuse light.



510  
 511 Figure 4. The impact of diffuse reflection coefficient ( $k$ ) on light distribution within a rice canopy. A:  
 512 Scatter plot of scattered photosynthetic photon flux density (PPFD) versus canopy height. B: Vertical  
 513 distribution of scattered PPFD across different canopy layers, presented as box plots. C: Mean scattered  
 514 PPFD at each canopy layer. D-E: Frequency distribution of scattered PPFD under (D)  $k=0.01$  and (E)  
 515  $k=0.35$ . F: Comparative histogram of scattered PPFD distributions for both scattering coefficients.

516 When varying the diffuse reflection coefficient ( $k$ ) between 0.01 and 0.35 while  
517 fixing leaf roughness ( $\sigma = 0.3$ ) and refractive index ( $n = 1$ ), marked differences were  
518 observed in the spatial patterns of scattered PPFD (Fig. 4A–C). Canopy upper layers  
519 exhibited substantially higher scattered PPFD under  $k = 0.35$  compared with  $k =$   
520 0.01. The proportion of leaf facets exposed to medium light intensity (40–80  
521  $\mu\text{mol m}^{-2} \text{s}^{-1}$ ) increased under low  $k$ , whereas the fraction under high light intensity  
522 (80–150  $\mu\text{mol m}^{-2} \text{s}^{-1}$ ) declined. These findings indicate that a lower diffuse  
523 reflection coefficient leads to a more homogeneous scattered light distribution within  
524 the canopy.

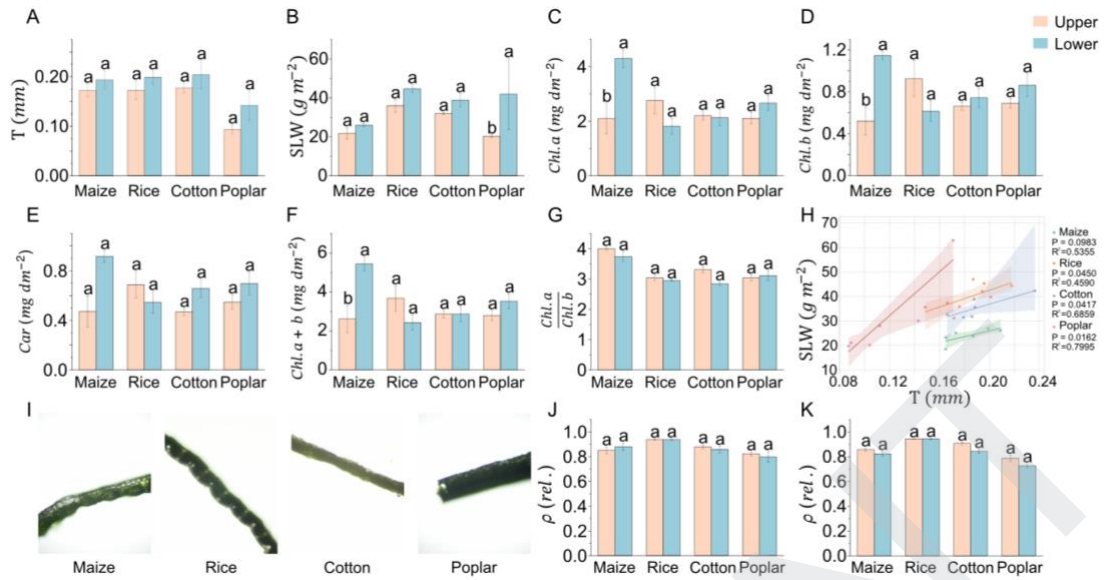
525 Further simulations altering  $\sigma$  (0.3 and 1.0) and  $n$  (1.0 and 2.2), as well as  
526 combined parameter sets (e.g.,  $k = 0.01$  with  $n = 1.0$ ,  $k = 0.35$  with  $n = 2.2$ ),  
527 showed that all three parameters substantially influence canopy-level radiation patterns  
528 (Fig. S9–S13). These results emphasize that accurate BRDF parameterization is  
529 essential for simulating canopy radiative transfer and photosynthesis.

### 530 **Variations of leaf anatomical and physiological traits at upper and lower canopy 531 layers in four species**

532 To study the relationship between leaf optical properties and leaf anatomical and  
533 physiological traits, we chose four species including two monocotyledonous (maize,  
534 rice) and two dicotyledonous (cotton, poplar). The leaves at both upper and lower layers  
535 of these plants' canopies were used for the measurement because the leaves acclimate  
536 to heterogeneous light environment in canopy. The phenotypic traits, including leaf  
537 thickness (T), specific leaf weight (SLW), chlorophyll a (*Chl. a*), chlorophyll b (*Chl. b*),  
538 and carotenoid content (*Car.*) were quantified. Two-way ANOVA revealed that both  
539 species and canopy layer had significant effects ( $P < 0.001$ ) on T and SLW (Table S3).  
540 However, *Chl. a*, *Chl. b*, and *Car.* contents were not significantly affected by either  
541 species or layer. Significant species and layer interactions were detected for *Chl. a*,  
542 *Chl. b*, and *Car.*, indicating that pigment-related traits exhibited species-dependent  
543 responses to canopy position.

544 The leaf thickness was not significantly different between upper and lower canopy

545 layers across species (**Fig. 5A**). SLW was significantly higher in lower-layer poplar  
546 leaves compared to upper-layer leaves ( $P < 0.05$ ) (**Fig. 5B**), possibly reflecting  
547 structural adaptations to lower light levels in the shaded canopy [62]. In contrast, SLW  
548 differences between canopy layers were less pronounced in maize, rice, and cotton. A  
549 positive correlation between SLW and T across species were observed, with poplar  
550 exhibiting the strongest correlation ( $R^2 > 0.79$ ) and rice the weakest ( $R^2 > 0.45$ ) (**Fig.**  
551 **5H**). The relationship between SLW and T was dramatically different among these four  
552 species, shown by the shaded areas representing the 95% confidence intervals,  
553 highlighting interspecies variation in leaf structure and density. We also calculated total  
554 chlorophyll (*Chl. a + b*) and the ratio of chlorophyll a to chlorophyll b (*Chl. a/Chl. b*).  
555 In maize, the chlorophyll content (*Chl. a* and *Chl. b*) was significantly higher in lower-  
556 layer leaves (**Fig. 5C-D, F**), but rice exhibited the opposite pattern. As shown in **Fig.**  
557 **5G**, the chlorophyll a/b ratio was not different between canopy layers. In maize, the  
558 *Car.* in lower-layer leaves nearly doubled that in upper-layer leaves (**Fig. 5E**). We also  
559 quantified the leaf surface roughness ( $\rho$ ) based on the leaf section images using the  
560 developed Roughness Calculator (RC) software (**Fig. 5I**). The results indicate that the  
561 position of the leaf within the canopy has no significant effect on the  $\rho$  of the leaf,  
562 with minimal differences between the adaxial (**Fig. 5J**) and abaxial (**Fig. 5K**) surfaces  
563 and consistent numerical trends. Rice leaves are the roughest, while poplar leaves are  
564 the smoothest.



565

566 Figure 5. Comparison of anatomical and physiological traits between upper- and lower-layer  
 567 canopy leaves across four plant species. A-G: leaf thickness, specific leaf weight, chlorophyll a,  
 568 chlorophyll b, carotenoid, total chlorophyll and chlorophyll a/b ratio in upper (red) and lower (blue)  
 569 canopy leaves of maize, rice, cotton and poplar. Data were presented as mean  $\pm$  SE (Standard Error).  
 570 Significant differences between canopy layers were determined using Two-way ANOVA with Bonferroni  
 571 multiple post-hoc tests, marked with \* for  $P < 0.05$ . H: linear regression between specific leaf weight  
 572 and thickness across four species, with 95% confidence intervals. The regression lines and coefficient of  
 573 determination ( $R^2$ ) values were provided for each species. I: leaf section microscopy image examples. J-  
 574 K: leaf surface roughness for the adaxial side (J) and abaxial side (K).

### 575 Spatial distribution of reflectance across species and canopy layers

576 Using the DSDI system developed in this study, we performed the measurement of  
 577 BRDF for the samples used for quantifying those anatomical and physiological traits  
 578 above. Both adaxial and abaxial surfaces of the leaves were measured. Then, the Cook  
 579 Torrance BRDF model was used to fit the data for deriving the BRDF parameters (Fig.  
 580 6). The reflectance distribution on leaf surfaces generally consists of a narrow peak (e.g.,  
 581 the blue ellipse in Fig. 1B) in the specular reflection direction, superimposed on a more  
 582 uniform diffuse background (e.g., the red semicircle in Fig. 1B) in the diffuse reflection  
 583 directions [37]. The maximum specular peak, indicative of nearly pure specular  
 584 reflection, reaches approximately  $0.6 \text{ sr}^{-1}$  within a small solid angle for poplar leaves  
 585 at light incident angle  $11\pi/36$  (Fig. 6). Notably, rice and cotton exhibit relatively  
 586 uniform reflectance distributions across both adaxial and abaxial surfaces, with lower  
 587 reflectance values compared to maize and poplar. This pattern may arise from specific

588 structural or biochemical properties in rice and cotton leaves that reduce directional  
589 reflection.

590 Interestingly, the peak of the BRDF appears at an angle slightly larger than the ideal  
591 specular reflection angle, an effect influenced by the  $\sigma(\lambda)$  [55]. Although the diffuse  
592 reflection component appears minor, it dominates when integrated over the entire  
593 hemisphere [37]. As the zenith illumination angle increases, all samples become more  
594 specular, with narrower and more pronounced BRDF peaks. Despite these common  
595 trends, the four species exhibit distinct BRDF profiles, allowing clear differentiation  
596 based on reflectance distribution patterns.

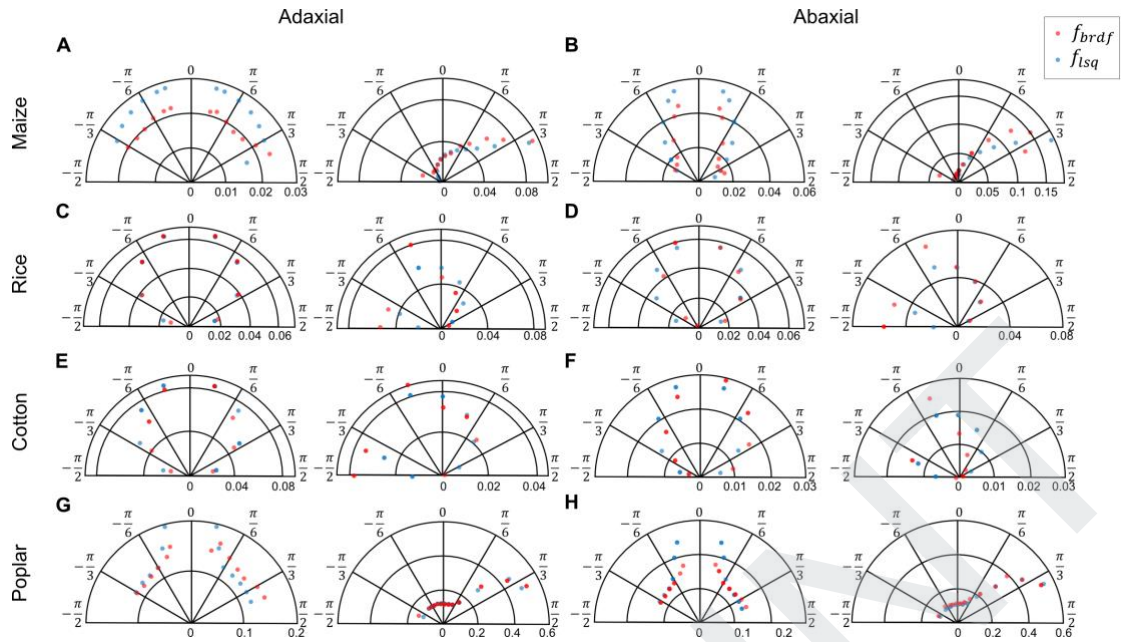
597 The polar plots in **Fig. 6** visualize these variations in reflectance distribution across  
598 species. Maize and poplar display pronounced specular reflections, particularly on the  
599 abaxial surfaces (**Fig. 6A-B, G-H**), while the BRDF peaks of rice and cotton ( $\approx 0.08$   
600  $\text{sr}^{-1}$ ) were significantly lower than those of maize ( $0.15 \text{ sr}^{-1}$ ) and poplar ( $0.6 \text{ sr}^{-1}$ ) ( $P <$   
601  $0.01$ ). (**Fig. 6C-F**). These findings underscore the importance of species-specific leaf  
602 surface adaptations in controlling light distribution within the canopy, with potential  
603 implications for enhancing photosynthetic efficiency. Such adaptations provide critical  
604 insights for refining light interaction models and highlight potential targets in breeding  
605 programs aiming at improving resource efficiency and productivity in diverse light  
606 environments.

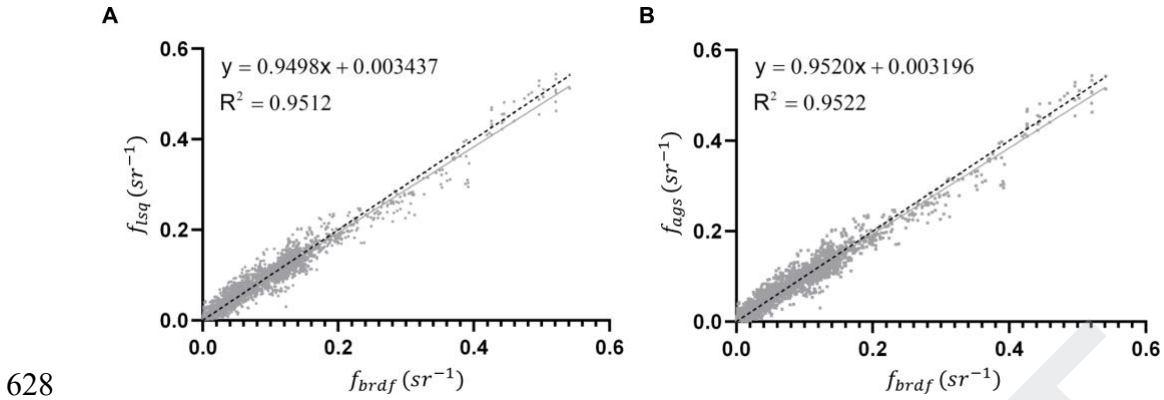
607

608 Figure 6. Reflectance distribution for the adaxial and abaxial surfaces of four species in polar coordinate.  
 609 The reflectance distributions for the adaxial (A, C, E, G) and abaxial (B, D, F, H) surfaces of leaves  
 610 across four plant species: maize (A-B), rice (C-D), cotton (E-F), and poplar (G-H). For each figure panel,  
 611 data of two illuminated angles (light incident angles) were shown. For maize and poplar, 0 (left) and  
 612  $11\pi/36$  (right) were shown, and for rice and cotton, 0 (left) and  $\pi/4$  (right) were shown. In the polar  
 613 coordinate, the angle represents the reflection angle, the radial represents the value of the BRDF, with  
 614 the pink asterisk representing the actual measured reflectance ( $f_{brdf}$ ) by the DSDI system and the green  
 615 circle representing the fitted reflectance ( $f_{lsq}$ ) on the BRDF model by the least squares curve fit. Units  
 616 of reflectance are given in  $sr^{-1}$ .

## 617 Evaluation of BRDF parameter fitting

618 To evaluate the performance of the BRDF parameter fitting, we applied two methods  
 619 ( $f_{lsq}$  for Least Squares and  $f_{ags}$  for Adaptive Grid Search) to fit the BRDF, based on  
 620 the actual measured reflectance of both leaf surfaces for upper and lower layer in  
 621 canopies of the four species. The fitted reflectance values ( $f_{lsq}$  and  $f_{ags}$ ) were linearly  
 622 correlated ( $R^2 = 0.9512$  and  $0.9522$ ) with the actual measured reflectance values ( $f_{brdf}$ )  
 623 (Fig. 7) at the measurement locations. Both methods provided high-quality fits to the  
 624 measured data ( $R^2 > 0.95$ ), effectively capturing the reflectance distribution on leaf  
 625 surfaces. While the Adaptive Grid Search achieved slightly higher fitting accuracy due  
 626 to its two-layer grid structure, but it required longer processing times. Therefore, we  
 627 used the results from the Least Squares fitting method for further analysis.





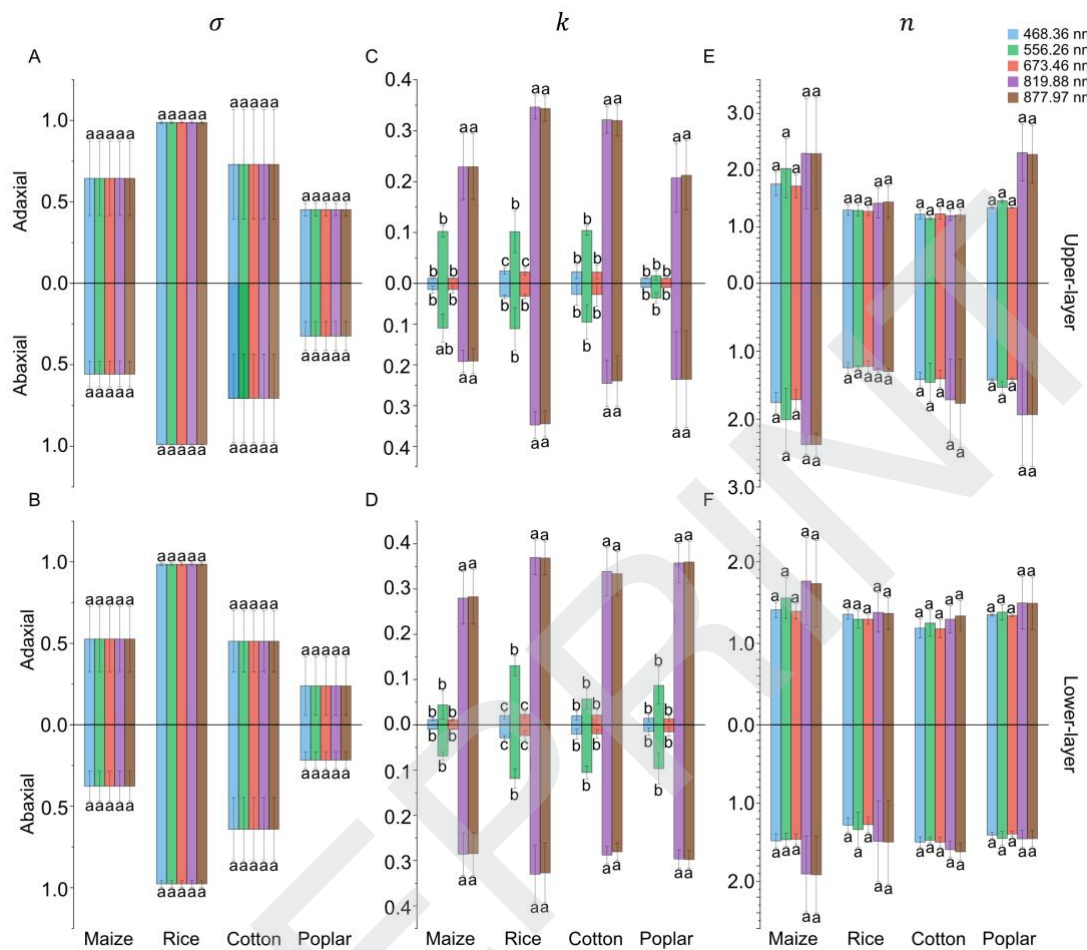
628

629 Figure 7. Comparison between measured and fitted BRDF values using two fitting methods, Least  
 630 Squares curve fit function (A) and the Adaptive Grid Search (B).  $f_{lsq}$  indicates BRDF values simulated  
 631 using the Least Squares fitting method, and  $f_{ags}$  denotes values derived from the Adaptive Grid  
 632 Search method. The black dotted line represents the 1:1 line, while the solid regression lines illustrate the  
 633 relationship between fitted bidirectional reflectance ( $f_{lsq}$  and  $f_{ags}$ ) and measured bidirectional reflectance  
 634 ( $f_{brdf}$ ). The coefficient of determination ( $R^2$ ) indicates the strength of correlation, with both methods  
 635 showing strong agreement with the measured data ( $R^2 > 0.95$ ). The scatter points present the  
 636 bidirectional reflectance for various combinations of incident angles and reflection angles.

### 637 Variations of BRDF Parameters Across Species and Canopy Layers

638 There were significant variations for BRDF parameters across species, canopy layers  
 639 and light wavelength (Fig. 8). Rice and cotton exhibited higher  $\sigma(\lambda)$  values than that  
 640 of maize and poplar for both two leaf surfaces and two canopy layers, indicating that  
 641 the rice and cotton had irregular surface structure compared to maize and poplar. This  
 642 higher roughness results in a relatively even reflectance distribution (Fig. 6C-F). In  
 643 contrast, maize and poplar show higher specular reflectance components (Fig. 6A-B,  
 644 G-H) due to their lower  $\sigma(\lambda)$  values, which increase the probability of concentrated  
 645 light reflection [63]. The  $\sigma(\lambda)$  was the same for different wavelengths, suggesting that  
 646 this parameter was a property of leaf surface texture controlled by species-specific  
 647 structural traits [64]. In contrast, the  $k(\lambda)$  demonstrates marked sensitivity to  
 648 wavelength, with the highest values at infrared region and relatively high at green light  
 649 and lower for blue and red light (Fig. 8C-D). This phenomenon can be explained by the  
 650 reflectance of leaf at these wavelengths. The wavelength-dependent nature of  $k(\lambda)$   
 651 aligns with general spectral reflectance properties, where longer wavelengths tend to  
 652 exhibit more diffuse scattering [51]. The  $n(\lambda)$  shows limited wavelength sensitivity  
 653 across species, with relatively high values in maize and poplar (Fig. 8E-F). Notably,

654  $n(\lambda)$  remains consistent between adaxial and abaxial surfaces, supported by the similar  
 655 structure of leaf surface at both side of a leaf.



656  
 657 **Figure 8.** Comparison of BRDF parameters across species (maize, rice, cotton, and poplar) and canopy  
 658 layers (upper and lower) for both adaxial and abaxial leaf surfaces. These parameters included roughness  
 659  $\sigma(\lambda)$  (A-B), diffuse reflectance coefficient  $k(\lambda)$  (C-D) and refractive index  $n(\lambda)$  (E-F). Each  
 660 parameter was measured at multiple wavelengths (468.36 nm, 556.26 nm, 673.46 nm, 819.88 nm  
 661 and 877.97 nm), represented by different colors. Data were presented as mean  $\pm$  SE (Standard Error)  
 662 for upper-layer (A, C, E) and lower-layer (B, D, F) leaves. Mean comparisons were conducted using  
 663 Tukey's HSD test at a significance level of 0.05. Different letters indicate significant differences among  
 664 different wavelengths.

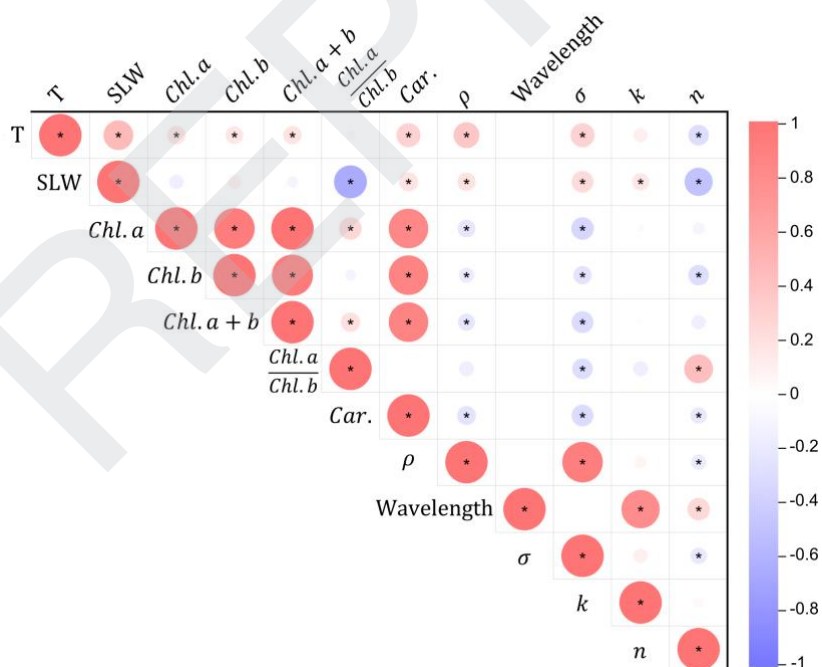
#### 665 Correlation Analysis Between Leaf Phenotypic Traits and BRDF Parameters

666 To further understand the relationship between leaf phenotypic traits and optical  
 667 properties, we performed a correlation analysis between relevant parameters, as  
 668 presented in **Fig. 9**. The analysis reveals a highly significant positive correlation  
 669 between  $\sigma(\lambda)$  and the leaf surface roughness  $\rho$ , with no significant correlation  
 670 between  $\sigma(\lambda)$  and wavelength. This finding suggests that  $\sigma(\lambda)$  primarily reflects the

671 intrinsic surface characteristics of the leaf, which can be reliably modeled through a  
 672 linear relationship based on  $\rho$  (Fig. S8). Additionally,  $\sigma(\lambda)$  shows a significant  
 673 negative correlation with pigment content.

674 The  $k(\lambda)$  was strong positive correlated with  $\lambda$ , consistent with known spectral  
 675 reflectance patterns in leaves, where light scattering generally increases with longer  
 676 wavelengths (from visible light to infrared light)[65]. It should be noted that  $k(\lambda)$  was  
 677 indeed correlated with the leaf absorbance for specific band of wavelength.

678 The  $n(\lambda)$  exhibits significant negative correlations with both T and SLW. This  
 679 indicates that denser and thicker leaves, which associated with higher SLW and T, tend  
 680 to have lower refractive indices, thereby reducing light transmittance. Furthermore,  
 681 there is a noteworthy negative correlation between  $\sigma(\lambda)$  and  $n(\lambda)$ , suggesting that as  
 682 surface roughness increases, the refractive index decreases. This relationship implies  
 683 that the leaf surface structure may be biologically connected to its internal composition,  
 684 potentially affecting its refractive properties [66].



685  
 686 **Figure 9.** Correlation matrix between wavelengths, leaf traits and BRDF parameters. This heatmap shows  
 687 the correlation coefficients among various parameters, including Leaf thickness (T), Specific leaf weight  
 688 (SLW), Chlorophyll a (*Chl.a*), Chlorophyll b (*Chl.b*), Carotenoid content (*Car.*), Total chlorophyll  
 689 (*Chl.a + b*), Ratio of chlorophyll a to b ((*Chl.a*)/(*Chl.b*)), leaf surface roughness ( $\rho$ ), measurement  
 690 wavelength ( $\lambda$ ), and the BRDF parameters  $\sigma(\lambda)$ ,  $k(\lambda)$ , and  $n(\lambda)$ . The wavelength feature represents  
 691 the spectral band (400–992 nm) at which BRDF parameters were measured. The color scale represents

692 the strength and direction of correlations, with red indicating positive correlations and blue indicating  
693 negative correlations. The color intensity and size of the circle correspond to the strength of the  
694 correlation, as shown in the color bar. Pearson's correlation coefficient was used, and significant  
695 correlations were marked with an asterisk (\*) at the  $P < 0.05$  level.

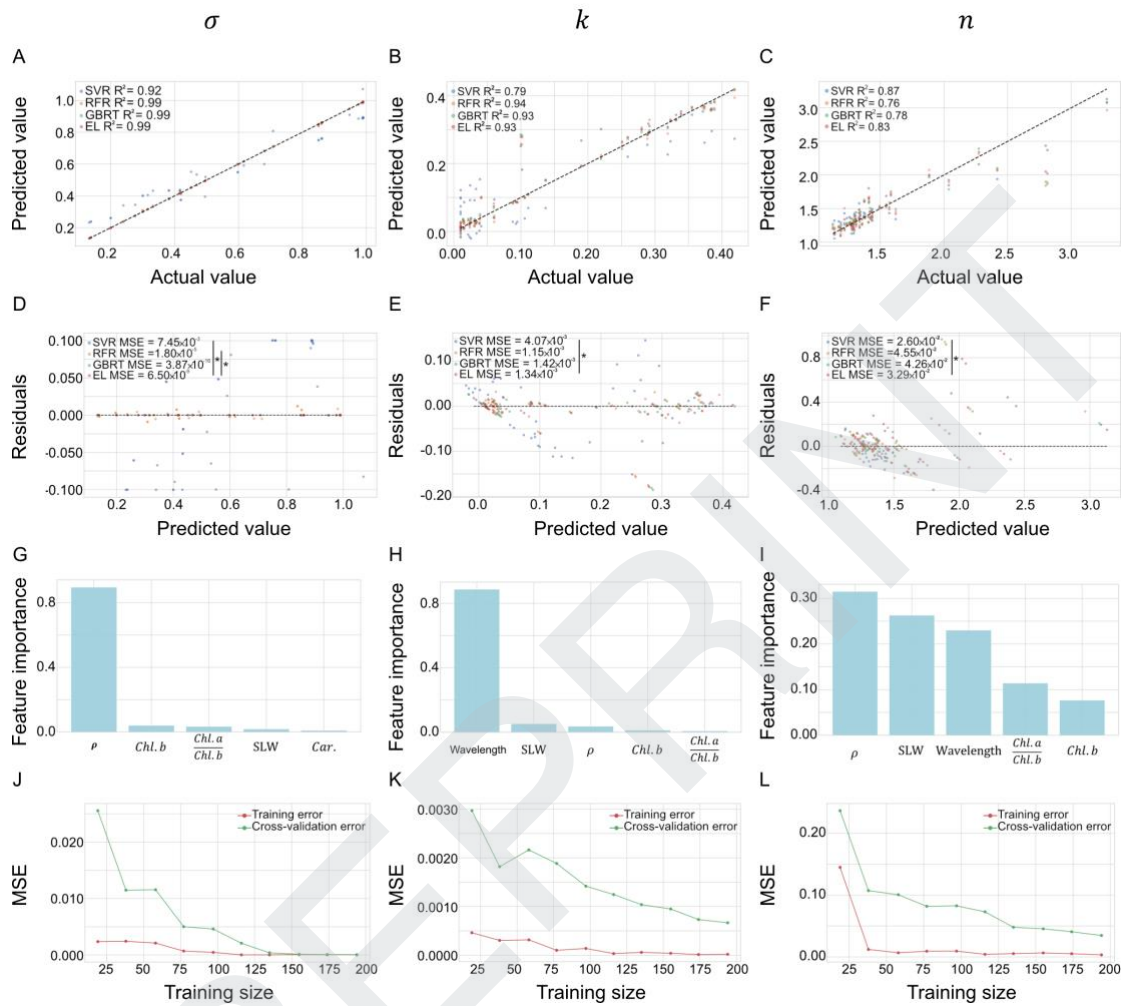
696 **Predictive model for BRDF parameters with data of leaf anatomical and**  
697 **physiological traits**

698 To predict the BRDF parameters using the data of leaf anatomical and physiological  
699 traits, several base models and the ensemble learning model were trained and evaluated.  
700 Results show that the  $R^2$  of stacking ensemble learning (EL) model was generally  
701 higher than individual base models, including Support Vector Regression (SVR),  
702 Random Forest Regression (RFR), and Gradient Boosting Regression Tree (GBRT), in  
703 predicting BRDF parameters ( $\sigma(\lambda)$ ,  $k(\lambda)$ , and  $n(\lambda)$ ). The comparison of models  
704 shows that the EL model consistently outperforms the individual models, yielding  $R^2$   
705 value 0.83-0.99 on the test set (Fig. 10A-C). However, all models demonstrated a  
706 relatively lower performance in predicting  $n(\lambda)$ , likely due to additional influencing  
707 factors, such as water content, which affect light transmission properties in leaves [26].

708 To assess statistical significance in model performance, paired t-tests were  
709 conducted. Fig. 10D-F reveals that the EL model had a significantly lower Mean  
710 Squared Error (MSE) than the SVR model ( $P < 0.05$ ), though differences between the  
711 EL model and RFR or GBRT were not statistically significant. Feature importance  
712 analysis (Fig. 10G-I) indicated that leaf surface roughness ( $\rho$ ) and wavelength ( $\lambda$ ) were  
713 the dominant predictors for BRDF parameters  $\sigma(\lambda)$ ,  $k(\lambda)$ , and  $n(\lambda)$ , followed by  
714 specific leaf weight (SLW) and pigment-related traits ((Chl.a)/(Chl.b) and Chl.b).  
715 These results suggest that both structural and spectral features play critical roles in  
716 determining leaf optical features. The learning curves (Fig. 10J-L) show the training  
717 and cross-validation error for each model, with the EL model achieving lower cross-  
718 validation error, indicating improved generalization capability for unseen data.

719 These findings confirm that the stacking EL model provides robust and accurate  
720 predictions for BRDF parameters by effectively integrating the strengths of each base  
721 model. The enhanced predictive power of the EL model offers a reliable framework for

722 modeling leaf optical properties based on leaf traits, which could be instrumental in  
 723 refining canopy light distribution models and optimizing crop canopy.



724  
 725 **Figure 10.** Performance of ensemble learning (EL) model for predicting BRDF parameters  $\sigma(\lambda)$ ,  $k(\lambda)$ ,  
 726 and  $n(\lambda)$  based on leaf traits. A-C: the scatter plots of actual versus predicted values for  $\sigma(\lambda)$ ,  $k(\lambda)$ ,  
 727 and  $n(\lambda)$ , respectively, with a dotted line indicating the 1:1 relationship. D-F: the residual plots for each  
 728 parameter, illustrating the residual distribution against predicted values. G-I: Importance of leaf  
 729 phenotypic traits for predicting BRDF parameters in RFR model. J-L: present the learning curves,  
 730 showing both training error (red line) and cross-validation error (green line) for the EL model during the  
 731 training process for each parameter. Model comparisons were based on SVR (Support Vector Regressor),  
 732 RFR (Random Forest Regressor), GBRT (Gradient Boosting Regressor), and a stacking EL model. The  
 733 statistical metrics (MSE and  $R^2$ ) indicate the accuracy and robustness of the models, with the stacking  
 734 model showing superior performance for most parameters. Statistical significance was assessed via  
 735 paired t-tests, with a significance level of  $P < 0.05$ , denoted by an asterisk (\*).  
 736

## 737 Discussion

738 This study introduces an integrated framework combining optical instrumentation  
 31

739 (DSDI), physics-based modeling (BRDF), and data-driven analytics (EL) to quantify  
740 and predict leaf optical properties from anatomical and biochemical traits. Unlike  
741 traditional optical methods limited to slow reflectance or transmittance measurements,  
742 the proposed approach transforms optical characterization into a phenotype-driven,  
743 scalable, and computationally extensible process. The DSDI system enables precise  
744 measurement of directional reflectance across multiple angles, and the derived BRDF  
745 parameters ( $\sigma$ ,  $k$ , and  $n$ ) capture critical variations in surface roughness, scattering,  
746 and refractive properties that define leaf optical diversity among species and canopy  
747 layers.

#### 748 **Integration of Optical Traits into Phenomics Frameworks**

749 Three-dimensional (3D) canopy photosynthesis models can be used to identify factors  
750 controlling canopy photosynthesis efficiency and deconvolute dominant factors  
751 governing canopy photosynthetic performance [67–70]. The distribution of direct light  
752 and diffuse light has been found to have a significant impact on the photosynthetic  
753 efficiency of the canopy [71]. Plant architectural traits, such as leaf type and leaf angle,  
754 also influences light distribution in plant canopy.

755 One of the major predictions of such canopy photosynthesis models is that canopy  
756 with vertical light-green leaves in upper canopy coupled with horizontal dark-green  
757 foliar arrangements in lower canopy can help increase efficiency [63]. Such a canopy  
758 architecture can enhance photon flux homogeneity, simultaneously mitigating light  
759 saturation in apical leaves while alleviating light limitations in basal leaves. In this study,  
760 leaf anatomical and biochemical features are major determinants of optical properties  
761 of the leaf [72,73]. Our results reveal a statistically robust correlation between the  
762 roughness parameter ( $\sigma(\lambda)$ ) of the BRDF model and leaf surface roughness ( $\rho$ ) derived  
763 from leaf cross-sectional microscopy quantifications (Fig. 9). The established linear  
764 regression model (Fig. S8) enables practical estimation of  $\sigma(\lambda)$  through rapid  $\rho$   
765 characterization using microscopy-based measurements. This positive correlation  
766 suggests that leaf surface irregularities directly influence BRDF roughness, likely  
767 enhancing light scattering within the canopy. A pronounced correlation was observed

768 between the diffuse reflection coefficient ( $k(\lambda)$ ) and wavelength (Fig. 9). This  
769 relationship aligns with the known wavelength dependence of leaf spectral reflectance  
770 [74]. The refractive index ( $n(\lambda)$ ) demonstrated a negative correlation with leaf  
771 thickness and specific leaf weight (Fig. 9). This finding suggests that thinner leaves in  
772 the upper layer tend to transmit more light, which could be advantageous in light  
773 distribution and utilization for the whole canopy, particularly for species such as maize  
774 and poplar [75]. These new observations provide a new dimension of crop canopy  
775 engineering, i.e. manipulating the leaf optical properties instead of canopy architectures  
776 for a better light environment inside a canopy for greater efficiency.

#### 777 **Effectiveness of the EL Model for Predicting Optical Properties**

778 Our ensemble learning (EL) model effectively predicted leaf optical properties ( $\sigma(\lambda)$ ,  
779  $k(\lambda)$  and  $n(\lambda)$ ) based on phenotypic traits, with high accuracy ( $R^2 > 0.83$  for all  
780 parameters, as shown in Fig. 10). However, the relative weaker predictive power  
781 for  $n(\lambda)$  ( $R^2 = 0.83$ ) suggests unaccounted factors, such as leaf water content [26] or  
782 other tissues [54], influence the leaf refractive index. The dominance of  $\rho$  highlights  
783 the critical role of epidermal microstructure in controlling the roughness parameter  
784  $\sigma(\lambda)$ , consistent with previous studies linking surface topology to directional scattering.  
785 The significant contribution of  $\lambda$  reflects the wavelength-dependent variation in  
786 pigment absorption and scattering, affecting both the diffuse reflection coefficient  
787  $k(\lambda)$  and refractive index  $n(\lambda)$ . Meanwhile, SLW and chlorophyll-related traits  
788 contributed secondarily, indicating that leaf thickness and pigment composition  
789 modulate internal light transmission and absorption. Together, these findings  
790 demonstrate that the EL model not only achieved accurate prediction but also captured  
791 biologically interpretable relationships between leaf structure, pigment composition,  
792 and BRDF parameters.

793

#### 794 **Biological Relevance and Future Directions**

795 Our findings underscore that leaf optical properties represent an important yet  
796 underutilized dimension of plant phenotyping. The correlations between BRDF

parameters and phenotypic traits such as leaf thickness, pigment composition, and surface microstructure highlight the potential of optical phenotyping to reveal functional adaptations of plant leaves. By integrating BRDF-predicted parameters into 3D canopy photosynthesis models, this framework enables virtual experiments for testing how structural or biochemical modifications affect canopy-scale light distribution, providing a foundation for data-driven crop ideotype design. Furthermore, when integrated with 3D point cloud data acquired from phenotyping platforms, the proposed method allows indirect scalable evaluation of canopy light distribution and photosynthetic efficiency, supporting computational phenotyping of canopy photosynthesis.

As the current dataset covers four representative species across two canopy positions, this limited biological diversity constrains the generalizability of the predictive model. The present study primarily focuses on developing an integrated hardware-software framework for predicting leaf optical properties from structural and biochemical traits, rather than achieving exhaustive species coverage. The selected species were chosen to represent both monocotyledonous and dicotyledonous groups, ensuring methodological diversity rather than taxonomic completeness. It is noteworthy that the prediction model for certain optical parameter, such as surface roughness ( $\sigma$ ), could be relatively conserved across species because they primarily depend on epidermal microstructure. In contrast, models for predicting parameters like the diffuse reflection coefficient ( $k$ ) and refractive index ( $n$ ) might exhibit species- and condition-specific variability, driven by biochemical composition and internal tissue organization.

Future studies should expand this framework across genotypes, environmental conditions, and stress treatments to construct universal predictive models for leaf optical behavior. The combination of optical phenotyping, machine learning, and radiative transfer modeling represents a promising direction for next-generation plant phenomics, where digital and computational tools jointly enable predictive understanding of plant function and light-use efficiency.

825 **Conclusion**

826 This study establishes an integrated framework that bridges optical physics and plant  
827 phenomics by combining a custom-designed Directional Spectrum Detection  
828 Instrument (DSDI), Bidirectional Reflectance Distribution Function (BRDF) modeling,  
829 and ensemble learning (EL) model. The framework enables accurate and scalable  
830 quantification of leaf optical properties and provides the predictive relationship  
831 between BRDF parameters and leaf phenotypic traits across multiple species. The  
832 DSDI system precisely measures directional reflectance, while roughness ( $\sigma$ ), diffuse  
833 reflection coefficient ( $k$ ), and refractive index ( $n$ ), capture key mechanisms governing  
834 leaf light scattering and absorption. The EL model achieved high prediction accuracy  
835 ( $R^2 = 0.83\text{--}0.99$ ), demonstrating that leaf structural and biochemical traits can reliably  
836 predict optical behavior. Ray-tracing simulations further confirmed that BRDF  
837 parameters strongly influence canopy light distribution, highlighting their importance  
838 for parameterizing 3D canopy photosynthesis models. Overall, this work advances  
839 phenomics-oriented optical characterization by linking measurable leaf traits to  
840 canopy-scale light modeling, providing a scalable, data-driven pathway toward  
841 predictive phenotyping and digital crop design for improved photosynthetic efficiency.

842 **Acknowledgments**

843 We would like to thank Jinze Hong, Hanyue Sun, Yunzhu Yu and Yuhui Liu for assistant  
844 of data measurements. **Funding:** We acknowledge the financial support of the National  
845 Natural Science Foundation of China (32270428) to Q.S., the Earmarked Fund for  
846 XJARS-Cotton (XJARS-03) to Y.Z., Open Project of the Key Laboratory of Oasis Eco-  
847 agriculture, Xinjiang Production and Construction Corps (202102) to Q.S.,  
848 the Strategic Priority Research Program of the Chinese Academy of  
849 Sciences (XDB0630300) to Q. S. and X. Z., the Shanghai Rising-Star Program  
850 (21QC1401200) to Q. S. . **Author Contributions:** X.Z. and Q.S. designed and  
851 conceived the study. Q.S. developed the equipment and ray tracing software. Q.S., L.M.,  
852 and Y.W. performed the experiments. L.X.Y., X.G., and M.W. developed software for

853 image analysis, L.D. and Q.S. analyzed the data, built models and wrote the paper with  
854 the inputs from all authors. Y.Z., Q.S., and X.Z. supervised the study. **Competing**  
855 **interests:** The authors declare that they have no competing interests.

856 **Data Availability**

857 The source code used in this study is available for noncommercial use and the code can  
858 be downloaded from <https://github.com/PlantSystemsBiology/brdf>. The updated ray  
859 tracing in this study is available for noncommercial use and the code can be downloaded  
860 from <https://github.com/PlantSystemsBiology/fastTracerPublic>. The data of this study  
861 are available from the corresponding author upon request.

862 **Supplementary Materials**

863 **Introduction for directional spectrum detection instrument developed in this**  
864 **study.**

865 **Figure S1.** Schematic diagram and photograph of the custom-built Directional  
866 Spectrum Detection Instrument (DSDI).

867 **Table S1.** HPX-2000 high-power xenon light source specifications.

868 **Table S2.** HR-2000 high-resolution fiber optic spectrometer specifications.

869 **Figure S2.** The reflect light intensity of standard white board at different zenith angles.

870 **Figure S3.** The relationship between the reflect light intensity of standard white-board  
871 and  $\cos(\theta)$ .

872 **Introduction for the roughness calculator software developed in this study.**

873 **Figure S4.** The interface of the RC software.

874 **Figure S5.** The pop-up interface of upload window.

875 **Figure S6.** The interface after calculated parameters of the whole region.

876 **Figure S7.** The interface after calculated parameters of the region of interest.

877 **Figure S8.** Correlation between leaf surface roughness ( $\rho$ ) and BRDF roughness  
878 parameter ( $\sigma(\lambda)$ ) for four plant species.

879 **Ray tracing simulations for evaluation of canopy scattered light distribution**

880 **Figure S9.** The impact of leaf roughness ( $\sigma$ ) on light distribution within a rice canopy.

881 **Figure S10.** The impact of refractive index ( $n$ ) on light distribution within a rice canopy  
882 ( $k=0.01$ ).

883 **Figure S11.** The impact of refractive index ( $n$ ) on light distribution within a rice canopy  
884 ( $k=0.35$ ).

885 **Figure S12.** The impact of diffuse reflection coefficient ( $k$ ) and Refractive index ( $n$ )  
886 on light distribution within a rice canopy ( $\sigma=0.3$ ).

887 **Figure S13.** The impact of diffuse reflection coefficient ( $k$ ) and refractive index ( $n$ ) on  
888 light distribution within a rice canopy ( $\sigma=1$ ).

889 **Summary statistics (mean  $\pm$  SE) and two-way ANOVA results showing the effects  
890 of species (S), canopy layer (L), and their interaction (S  $\times$  L).**

891 **Table S3.** Leaf structural and biochemical traits across upper and lower canopy layers  
892 for maize, rice, cotton, and poplar.

893    **References**

- 894    1 Song, Q., Van Rie, J., Den Boer, B., Galle, A., Zhao, H., Chang, T., He, Z. and  
895    Zhu, X.-G. (2022) Diurnal and Seasonal Variations of Photosynthetic Energy  
896    Conversion Efficiency of Field Grown Wheat. *Frontiers in Plant Science*,  
897    Frontiers, **13**. <https://doi.org/10.3389/fpls.2022.817654>.
- 898    2 Digrado, A., Mitchell, N.G., Montes, C.M., Dirvanskyte, P. and Ainsworth, E.A.  
899    (2020) Assessing Diversity in Canopy Architecture, Photosynthesis, and Water-  
900    use Efficiency in a Cowpea Magic Population. *Food and Energy Security*, **9**, e236.  
901    <https://doi.org/10.1002/fes3.236>.
- 902    3 Huber, M., Nieuwendijk, N.M., Pantazopoulou, C.K. and Pierik, R. (2021) Light  
903    Signalling Shapes Plant–Plant Interactions in Dense Canopies. *Plant, Cell &*  
904    *Environment*, **44**, 1014–1029. <https://doi.org/10.1111/pce.13912>.
- 905    4 Sultana, F., Dev, W., Xin, M., Han, Y., Feng, L., Lei, Y., Yang, B., Wang, G., Li,  
906    X., Wang, Z., Xing, F., Xiong, S. and Li, Y. (2023) Competition for Light  
907    Interception in Different Plant Canopy Characteristics of Diverse Cotton Cultivars.  
908    *Genes*, **14**, 364. <https://doi.org/10.3390/genes14020364>.
- 909    5 Yang, F., Liu, Q., Cheng, Y., Feng, L., Wu, X., Fan, Y., Raza, M.A., Wang, X.,  
910    Yong, T., Liu, W., Liu, J., Du, J., Shu, K. and Yang, W. (2020) Low Red/Far-Red  
911    Ratio as a Signal Promotes Carbon Assimilation of Soybean Seedlings by  
912    Increasing the Photosynthetic Capacity. *BMC Plant Biology*, **20**, 148.  
913    <https://doi.org/10.1186/s12870-020-02352-0>.
- 914    6 Croce, R., Carmo-Silva, E., Cho, Y.B., Ermakova, M., Harbinson, J., Lawson, T.,  
915    McCormick, A.J., Niyogi, K.K., Ort, D.R., Patel-Tupper, D., Pesaresi, P., Raines,  
916    C., Weber, A.P.M. and Zhu, X.-G. (2024) Perspectives on Improving  
917    Photosynthesis to Increase Crop Yield. *The Plant Cell*, koae132.  
918    <https://doi.org/10.1093/plcell/koae132>.
- 919    7 Long, S.P., Marshall-Colon, A. and Zhu, X.-G. (2015) Meeting the Global Food  
920    Demand of the Future by Engineering Crop Photosynthesis and Yield Potential.  
921    *Cell*, **161**, 56–66. <https://doi.org/10.1016/j.cell.2015.03.019>.
- 922    8 Xiao, F., Li, W., Xiao, M., Yang, Z., Cheng, W., Gao, S., Li, G., Ding, Y., Paul,  
923    M.J. and Liu, Z. (2021) A Novel Light Interception Trait of a Hybrid Rice Ideotype  
924    Indicative of Leaf to Panicle Ratio. *Field Crops Research*, **274**, 108338.  
925    <https://doi.org/10.1016/j.fcr.2021.108338>.
- 926    9 Gong, F., Wu, X., Zhang, H., Chen, Y. and Wang, W. (2015) Making Better Maize  
927    Plants for Sustainable Grain Production in a Changing Climate. *Frontiers in Plant  
928    Science*, Frontiers, **6**. <https://doi.org/10.3389/fpls.2015.00835>.
- 929    10 Lyu, X., Mu, R. and Liu, B. (2023) Shade Avoidance Syndrome in Soybean and  
930    Ideotype toward Shade Tolerance. *Molecular Breeding*, **43**, 31.  
931    <https://doi.org/10.1007/s11032-023-01375-3>.
- 932    11 Roth, L., Barendregt, C., Bétrix, C.-A., Hund, A. and Walter, A. (2022) High-  
933    Throughput Field Phenotyping of Soybean: Spotting an Ideotype. *Remote Sensing  
934    of Environment*, Elsevier, **269**, 112797. <https://doi.org/10.1016/j.rse.2021.112797>.
- 935    12 Carbajal-Friedrich, A.A.J. and Burgess, A.J. (2024) The Role of the Ideotype in

- 936 Future Agricultural Production. *Frontiers in Plant Physiology*, Frontiers, **2**.  
937 <https://doi.org/10.3389/fphgy.2024.1341617>.
- 938 13 Loison, R., Audebert, A., Debaeke, P., Hoogenboom, G., Leroux, L., Oumarou, P.  
939 and Gérardeaux, E. (2017) Designing Cotton Ideotypes for the Future: Reducing  
940 Risk of Crop Failure for Low Input Rainfed Conditions in Northern Cameroon.  
941 *European Journal of Agronomy*, Elsevier, **90**, 162–173.  
942 <https://doi.org/10.1016/j.eja.2017.08.003>.
- 943 14 Burgess, A.J., Retkute, R., Herman, T. and Murchie, E.H. (2017) Exploring  
944 Relationships between Canopy Architecture, Light Distribution, and  
945 Photosynthesis in Contrasting Rice Genotypes Using 3D Canopy Reconstruction.  
946 *Frontiers in Plant Science*, Frontiers, **8**. <https://doi.org/10.3389/fpls.2017.00734>.
- 947 15 Tang, L., Yin, D., Chen, S., Chen, C., Huang, H. and Lin, D. (2017) Virtual  
948 Geographic Simulation of Light Distribution within Three-Dimensional Plant  
949 Canopy Models. *ISPRS International Journal of Geo-Information*, **6**, 405.  
950 <https://doi.org/10.3390/ijgi6120405>.
- 951 16 Chang, T.-G., Zhao, H., Wang, N., Song, Q.-F., Xiao, Y., Qu, M. and Zhu, X.-G.  
952 (2019) A Three-Dimensional Canopy Photosynthesis Model in Rice with a  
953 Complete Description of the Canopy Architecture, Leaf Physiology, and  
954 Mechanical Properties. *Journal of Experimental Botany*, **70**, 2479–2490.  
955 <https://doi.org/10.1093/jxb/ery430>.
- 956 17 Burgess, A.J., Retkute, R., Pound, M.P., Mayes, S. and Murchie, E.H. (2017)  
957 Image-Based 3D Canopy Reconstruction to Determine Potential Productivity in  
958 Complex Multi-Species Crop Systems. *Annals of Botany*, Oxford Academic, **119**,  
959 517–532. <https://doi.org/10.1093/aob/mcw242>.
- 960 18 Zhu, R., Sun, K., Yan, Z., Yan, X., Yu, J., Shi, J., Hu, Z., Jiang, H., Xin, D., Zhang,  
961 Z., Li, Y., Qi, Z., Liu, C., Wu, X. and Chen, Q. (2020) Analysing the Phenotype  
962 Development of Soybean Plants Using Low-Cost 3D Reconstruction. *Scientific  
963 Reports*, Nature Publishing Group, **10**, 7055. [https://doi.org/10.1038/s41598-020-63720-2](https://doi.org/10.1038/s41598-020-<br/>964 63720-2).
- 965 19 Jin, S., Su, Y., Gao, S., Wu, F., Hu, T., Liu, J., Li, W., Wang, D., Chen, S., Jiang,  
966 Y., Pang, S. and Guo, Q. (2018) Deep Learning: Individual Maize Segmentation  
967 from Terrestrial Lidar Data Using Faster R-CNN and Regional Growth  
968 Algorithms. *Frontiers in Plant Science*, **9**, 866.  
969 <https://doi.org/10.3389/fpls.2018.00866>.
- 970 20 Sun, S., Li, C., Chee, P.W., Paterson, A.H., Meng, C., Zhang, J., Ma, P., Robertson,  
971 J.S. and Adhikari, J. (2021) High Resolution 3D Terrestrial LiDAR for Cotton  
972 Plant Main Stalk and Node Detection. *Computers and Electronics in Agriculture*,  
973 **187**, 106276. <https://doi.org/10.1016/j.compag.2021.106276>.
- 974 21 Slattery, R.A. and Ort, D.R. (2021) Perspectives on Improving Light Distribution  
975 and Light Use Efficiency in Crop Canopies. *Plant Physiology*, **185**, 34–48.  
976 <https://doi.org/10.1093/plphys/kiaa006>.
- 977 22 Zhang, J., Zhang, Z., Neng, F., Xiong, S., Wei, Y., Cao, R., Wei, Q., Ma, X. and  
978 Wang, X. (2022) Canopy Light Distribution Effects on Light Use Efficiency in  
979 Wheat and Its Mechanism. *Frontiers in Ecology and Evolution*, Frontiers, **10**.

- 980 https://doi.org/10.3389/fevo.2022.1023117.
- 981 23 Gandilyan, D.V., Levashova, N.T. and Olchev, A.V. (2020) Application of Monte  
982 Carlo Method for Modeling Reflection and Transmission of Solar Radiation by  
983 the Forest Canopy. *Moscow University Physics Bulletin*, **75**, 570–577.  
984 https://doi.org/10.3103/S0027134920060090.
- 985 24 Zhao, F., Dai, X., Verhoef, W., Guo, Y., Van Der Tol, C., Li, Y. and Huang, Y.  
986 (2016) FluorWPS: A Monte Carlo Ray-Tracing Model to Compute Sun-Induced  
987 Chlorophyll Fluorescence of Three-Dimensional Canopy. *Remote Sensing of  
988 Environment*, **187**, 385–399. https://doi.org/10.1016/j.rse.2016.10.036.
- 989 25 Fu, P., Meacham-Hensold, K., Guan, K., Wu, J. and Bernacchi, C. (2020)  
990 Estimating Photosynthetic Traits from Reflectance Spectra: A Synthesis of  
991 Spectral Indices, Numerical Inversion, and Partial Least Square Regression. *Plant,  
992 Cell & Environment*, **43**, 1241–1258. https://doi.org/10.1111/pce.13718.
- 993 26 Ustin, S.L. and Jacquemoud, S. (2020) How the Optical Properties of Leaves  
994 Modify the Absorption and Scattering of Energy and Enhance Leaf Functionality.  
995 In: Cavender-Bares, J., Gamon, J.A. and Townsend, P.A., Eds., *Remote Sensing  
996 of Plant Biodiversity*, Springer International Publishing, Cham, 349–384.  
997 https://doi.org/10.1007/978-3-030-33157-3\_14.
- 998 27 Yang, B., Knyazikhin, Y., Xie, D., Zhao, H., Zhang, J. and Wu, Y. (2018) Influence  
999 of Leaf Specular Reflection on Canopy Radiative Regime Using an Improved  
1000 Version of the Stochastic Radiative Transfer Model. *Remote Sensing*,  
1001 Multidisciplinary Digital Publishing Institute, **10**, 1632.  
1002 https://doi.org/10.3390/rs10101632.
- 1003 28 Bahrami, M. and Mobasher, M.R. (2020) Plant Species Determination by Coding  
1004 Leaf Reflectance Spectrum and Its Derivatives. *European Journal of Remote  
1005 Sensing*, Taylor & Francis.  
1006 https://www.tandfonline.com/doi/abs/10.1080/22797254.2020.1816501.
- 1007 29 Knapp, A. and Carter, G. (1998) Variability in Leaf Optical Properties among 26  
1008 Species from a Broad Range of Habitats. *American Journal of Botany*, **85**, 940.
- 1009 30 Krafft, D., Scarboro, C.G., Hsieh, W., Doherty, C., Balint-Kurti, P. and Kudenov,  
1010 M. (2024) Mitigating Illumination-, Leaf-, and View-Angle Dependencies in  
1011 Hyperspectral Imaging Using Polarimetry. *Plant Phenomics*, **6**, 0157.  
1012 https://doi.org/10.34133/plantphenomics.0157.
- 1013 31 Cao, Y., Zhong, Z., Wang, H. and Shen, R. (2022) Leaf Angle: A Target of Genetic  
1014 Improvement in Cereal Crops Tailored for High-density Planting. *Plant  
1015 Biotechnology Journal*, **20**, 426–436. https://doi.org/10.1111/pbi.13780.
- 1016 32 Zhao, X., Qi, J., Yu, Z., Yuan, L. and Huang, H. (2024) Fine-Scale Quantification  
1017 of Absorbed Photosynthetically Active Radiation (APAR) in Plantation Forests  
1018 with 3D Radiative Transfer Modeling and LiDAR Data. *Plant Phenomics*,  
1019 American Association for the Advancement of Science, **6**, 0166.  
1020 https://doi.org/10.34133/plantphenomics.0166.
- 1021 33 Combes, D., Bousquet, L., Jacquemoud, S., Sinoquet, H., Varlet-Grancher, C. and  
1022 Moya, I. (2007) A New Spectrogoniophotometer to Measure Leaf Spectral and  
1023 Directional Optical Properties. *Remote Sensing of Environment*, **109**, 107–117.

- 1024 https://doi.org/10.1016/j.rse.2006.12.007.
- 1025 34 Xu, K. and Ye, H. (2023) Light Scattering in Stacked Mesophyll Cells Results in  
1026 Similarity Characteristic of Solar Spectral Reflectance and Transmittance of  
1027 Natural Leaves. *Scientific Reports*, **13**, 4694. https://doi.org/10.1038/s41598-023-  
1028 31718-1.
- 1029 35 Kallel, A. (2018) Leaf Polarized BRDF Simulation Based on Monte Carlo 3-D  
1030 Vector RT Modeling. *Journal of Quantitative Spectroscopy and Radiative  
1031 Transfer*, **221**, 202–224. https://doi.org/10.1016/j.jqsrt.2018.09.033.
- 1032 36 Bousquet, L., Lachérade, S., Jacquemoud, S. and Moya, I. (2005) Leaf BRDF  
1033 Measurements and Model for Specular and Diffuse Components Differentiation.  
1034 *Remote Sensing of Environment*, **98**, 201–211.  
1035 https://doi.org/10.1016/j.rse.2005.07.005.
- 1036 37 Roth, B.D., Saunders, M.G., Bachmann, C.M. and van Aardt, J.A. (2020) On Leaf  
1037 BRDF Estimates and Their Fit to Microfacet Models. *IEEE Journal of Selected  
1038 Topics in Applied Earth Observations and Remote Sensing*, **13**, 1761–1771.  
1039 https://doi.org/10.1109/JSTARS.2020.2988428.
- 1040 38 Yao, C., Sun, Z. and Lu, S. (2022) Reducing BRDF Effects on the Estimation of  
1041 Leaf Biochemical Parameters Using the Nonpolarized Reflectance Factor in the  
1042 Hemispheric Space. *IEEE Transactions on Geoscience and Remote Sensing*, **60**,  
1043 1–17. https://doi.org/10.1109/TGRS.2022.3175721.
- 1044 39 Earles, J.M., Theroux-Rancourt, G., Roddy, A.B., Gilbert, M.E., McElrone, A.J.  
1045 and Brodersen, C.R. (2018) Beyond Porosity: 3D Leaf Intercellular Airspace  
1046 Traits That Impact Mesophyll Conductance. *Plant Physiology*, **178**, 148–162.  
1047 https://doi.org/10.1104/pp.18.00550.
- 1048 40 Chen, M. and Weng, F. Kramers-kronig Analysis of Leaf Refractive Index with  
1049 the PROSPECT Leaf Optical Property Model.  
1050 https://doi.org/10.1029/2012JD017477.
- 1051 41 Fox, J. and Weisberg, S. (2019) An R Companion to Applied Regression. 3rd ed.,  
1052 Sage, Thousand Oaks CA. https://www.john-fox.ca/Companion/.
- 1053 42 Lenth, R.V. (2025) Emmeans: Estimated Marginal Means, Aka Least-Squares  
1054 Means. manual. https://CRAN.R-project.org/package=emmeans.
- 1055 43 Kassambara, A. (2023) Rstatix: Pipe-Friendly Framework for Basic Statistical  
1056 Tests. manual. https://github.com/kassambara/rstatix.
- 1057 44 Pedregosa, F., Varoquaux, G., Gramfort, A., Michel, V., Thirion, B., Grisel, O.,  
1058 Blondel, M., Prettenhofer, P., Weiss, R., Dubourg, V., and Others. (2011) Scikit-  
1059 Learn: Machine Learning in Python. *Journal of Machine Learning Research*, **12**,  
1060 2825–2830.
- 1061 45 Song, Q., Zhang, G. and Zhu, X.-G. (2013) Optimal Crop Canopy Architecture to  
1062 Maximise Canopy Photosynthetic CO<sub>2</sub> Uptake under Elevated CO<sub>2</sub> – a  
1063 Theoretical Study Using a Mechanistic Model of Canopy Photosynthesis.  
1064 *Functional Plant Biology*, **40**, 108. https://doi.org/10.1071/FP12056.
- 1065 46 Comar, A., Baret, F., Obein, G., Simonot, L., Meneveaux, D., Viénot, F. and de  
1066 Solan, B. (2014) ACT: A Leaf BRDF Model Taking into Account the Azimuthal  
1067 Anisotropy of Monocotyledonous Leaf Surface. *Remote Sensing of Environment*,

- 1068 143, 112–121. <https://doi.org/10.1016/j.rse.2013.12.006>.
- 1069 47 Folkesson, J., Chang, H. and Bore, N. (2020) Lambert's Cosine Law and Sidescan  
1070 Sonar Modeling. 2020 IEEE/OES Autonomous Underwater Vehicles Symposium  
1071 (AUV), 1–6. <https://doi.org/10.1109/AUV50043.2020.9267946>.
- 1072 48 Weik, M.H. (2001) Lambert's Cosine Law. In: Weik, M.H., Ed., Computer Science  
1073 and Communications Dictionary, Springer US, Boston, MA, 868–868.  
1074 [https://doi.org/10.1007/1-4020-0613-6\\_9901](https://doi.org/10.1007/1-4020-0613-6_9901).
- 1075 49 Comar, A., Baret, F., Viénot, F., Yan, L. and de Solan, B. (2012) Wheat Leaf  
1076 Bidirectional Reflectance Measurements: Description and Quantification of the  
1077 Volume, Specular and Hot-Spot Scattering Features. *Remote Sensing of*  
1078 *Environment*, **121**, 26–35. <https://doi.org/10.1016/j.rse.2011.01.028>.
- 1079 50 Li, Y., Yang, P., Bai, L. and Zhang, Z. (2023) BRDF Modeling and Optimization  
1080 of a Target Surface Based on the Gradient Descent Algorithm. *Applied Optics*,  
1081 Optica Publishing Group, **62**, 9486–9492. <https://doi.org/10.1364/AO.506672>.
- 1082 51 Schaepman-Strub, G., Schaepman, M.E., Painter, T.H., Dangel, S. and Martonchik,  
1083 J.V. (2006) Reflectance Quantities in Optical Remote Sensing—Definitions and  
1084 Case Studies. *Remote Sensing of Environment*, **103**, 27–42.  
1085 <https://doi.org/10.1016/j.rse.2006.03.002>.
- 1086 52 Cook, R.L. (1981) A REFLECTANCE MODEL FOR COMPUTER GRAPHICS.  
1087 *Computer Graphics*, **15**.
- 1088 53 Brakke, T.W. (1994) Specular and Diffuse Components of Radiation Scattered by  
1089 Leaves. *Agricultural and Forest Meteorology*, **71**, 283–295.  
1090 [https://doi.org/10.1016/0168-1923\(94\)90016-7](https://doi.org/10.1016/0168-1923(94)90016-7).
- 1091 54 Karabourniotis, G., Liakopoulos, G., Bresta, P. and Nikolopoulos, D. (2021) The  
1092 Optical Properties of Leaf Structural Elements and Their Contribution to  
1093 Photosynthetic Performance and Photoprotection. *Plants*, **10**, 1455.  
1094 <https://doi.org/10.3390/plants10071455>.
- 1095 55 Meneveau, D., Bringier, B., Tauzia, E., Ribardiere, M. and Simonot, L. (2018)  
1096 Rendering Rough Opaque Materials with Interfaced Lambertian Microfacets.  
1097 *IEEE Transactions on Visualization and Computer Graphics*, **24**, 1368–1380.  
1098 <https://doi.org/10.1109/TVCG.2017.2660490>.
- 1099 56 Butler, S.D., Nauyoks, S.E. and Marciniak, M.A. (2015) Comparison of  
1100 Microfacet BRDF Model to Modified Beckmann-Kirchhoff BRDF Model for  
1101 Rough and Smooth Surfaces. *Optics Express*, Optica Publishing Group, **23**,  
1102 29100–29112. <https://doi.org/10.1364/OE.23.029100>.
- 1103 57 Liu, H., Zhu, J. and Wang, K. (2015) Modified Polarized Geometrical Attenuation  
1104 Model for Bidirectional Reflection Distribution Function Based on Random  
1105 Surface Microfacet Theory. *Optics Express*, Optica Publishing Group, **23**, 22788–  
1106 22799. <https://doi.org/10.1364/OE.23.022788>.
- 1107 58 Wittmann, B., Montmitonnet, P., Burr, A., Gauthier, C., Agassant, J.-F. and Casoli,  
1108 A. (2021) BRDF and Gloss Computation of Polyurethane Coatings from  
1109 Roughness Measurements: Modelling and Experimental Validation. *Progress in*  
1110 *Organic Coatings*, **156**, 106247. <https://doi.org/10.1016/j.porgcoat.2021.106247>.
- 1111 59 Berger, K., Reshetouski, I., Magnor, M. and Ihrke, I. (2011) Refractive Index

- 1112 Dependent Bidirectional Scattering Distribution Functions. ACM SIGGRAPH  
1113 2011 Posters, ACM, Vancouver British Columbia Canada, 1–1.  
1114 <https://doi.org/10.1145/2037715.2037789>.
- 1115 60 Thomas, D.J., Rainbow, J. and Bartley, L.E. (2023) The Rapid-Tome, a 3D-Printed  
1116 Microtome, and an Updated Hand-Sectioning Method for High-Quality Plant  
1117 Sectioning. *Plant Methods*, **19**, 12. <https://doi.org/10.1186/s13007-023-00986-3>.
- 1118 61 Guo, X., Shakeel, M., Wang, D., Qu, C., Yang, S., Ahmad, S. and Song, Z. (2022)  
1119 Metabolome and Transcriptome Profiling Unveil the Mechanisms of Light-  
1120 Induced Anthocyanin Synthesis in Rabbiteye Blueberry (*Vaccinium Ashei*:  
1121 Reade). *BMC Plant Biology*, **22**, 223. <https://doi.org/10.1186/s12870-022-03585-x>.
- 1122 62 Al Afas, N., Marron, N. and Ceulemans, R. (2007) Variability in *Populus* Leaf  
1123 Anatomy and Morphology in Relation to Canopy Position, Biomass Production,  
1124 and Varietal Taxon. *Annals of Forest Science*, **64**, 521–532.  
1125 <https://doi.org/10.1051/forest:2007029>.
- 1126 63 Nozka, L., Pech, M., Hiklova, H., Mandat, D., Hrabovsky, M., Schovanek, P. and  
1127 Palatka, M. (2011) BRDF Profile of Tyvek and Its Implementation in the Geant4  
1128 Simulation Toolkit. *Optics Express*, Optica Publishing Group, **19**, 4199–4209.  
1129 <https://doi.org/10.1364/OE.19.004199>.
- 1130 64 Zhang, Z., Liu, F., Zhou, Z., He, Y. and Fang, H. (2021) Roughness Measurement  
1131 of Leaf Surface Based on Shape from Focus. *Plant Methods*, **17**, 72.  
1132 <https://doi.org/10.1186/s13007-021-00773-y>.
- 1133 65 Wan, L., Zhang, J., Xu, Y., Huang, Y., Zhou, W., Jiang, L., He, Y. and Cen, H.  
1134 (2021) PROSDM: Applicability of PROSPECT Model Coupled with Spectral  
1135 Derivatives and Similarity Metrics to Retrieve Leaf Biochemical Traits from  
1136 Bidirectional Reflectance. *Remote Sensing of Environment*, **267**, 112761.  
1137 <https://doi.org/10.1016/j.rse.2021.112761>.
- 1138 66 Baker, R.L., Yarkhunova, Y., Vidal, K., Ewers, B.E. and Weinig, C. (2017)  
1139 Polyploidy and the Relationship between Leaf Structure and Function:  
1140 Implications for Correlated Evolution of Anatomy, Morphology, and Physiology  
1141 in *Brassica*. *BMC Plant Biology*, **17**, 3. <https://doi.org/10.1186/s12870-016-0957-3>.
- 1142 67 Gu, S., Wen, W., Xu, T., Lu, X., Yu, Z., Guo, X. and Zhao, C. (2022) Use of 3D  
1143 Modeling to Refine Predictions of Canopy Light Utilization: A Comparative Study  
1144 on Canopy Photosynthesis Models with Different Dimensions. *Frontiers in Plant  
1145 Science*, Frontiers, **13**. <https://doi.org/10.3389/fpls.2022.735981>.
- 1146 68 Liu, F., Song, Q., Zhao, J., Mao, L., Bu, H., Hu, Y. and Zhu, X. (2021) Canopy  
1147 Occupation Volume as an Indicator of Canopy Photosynthetic Capacity. *New  
1148 Phytologist*, **232**, 941–956. <https://doi.org/10.1111/nph.17611>.
- 1149 69 Song, Q., Liu, F., Bu, H. and Zhu, X.-G. (2023) Quantifying Contributions of  
1150 Different Factors to Canopy Photosynthesis in 2 Maize Varieties: Development of  
1151 a Novel 3D Canopy Modeling Pipeline. *Plant Phenomics*, **5**, 0075.  
1152 <https://doi.org/10.34133/plantphenomics.0075>.
- 1153 70 Wu, S., Wen, W., Wang, Y., Fan, J., Wang, C., Gou, W. and Guo, X. (2020) MVS-  
1154

- 1156 Pheno: A Portable and Low-Cost Phenotyping Platform for Maize Shoots Using  
1157 Multiview Stereo 3D Reconstruction. *Plant Phenomics*, **2020**, 2020/1848437.  
1158 <https://doi.org/10.34133/2020/1848437>.
- 1159 71 Williams, M., Rastetter, E.B., Van Der Pol, L. and Shaver, G.R. (2014) Arctic  
1160 Canopy Photosynthetic Efficiency Enhanced under Diffuse Light, Linked to a  
1161 Reduction in the Fraction of the Canopy in Deep Shade. *New Phytologist*, **202**,  
1162 1267–1276. <https://doi.org/10.1111/nph.12750>.
- 1163 72 Theiß, M., Steier, A., Rascher, U. and Müller-Linow, M. (2024) Completing the  
1164 Picture of Field-Grown Cereal Crops: A New Method for Detailed Leaf Surface  
1165 Models in Wheat. *Plant Methods*, **20**, 21. <https://doi.org/10.1186/s13007-023-01130-x>.
- 1166 73 Wu, A., Truong, S.H., McCormick, R., Van Oosterom, E.J., Messina, C.D., Cooper,  
1167 M. and Hammer, G.L. (2024) Contrasting Leaf-scale Photosynthetic Low-light  
1168 Response and Its Temperature Dependency Are Key to Differences in Crop-scale  
1169 Radiation Use Efficiency. *New Phytologist*, **241**, 2435–2447.  
1170 <https://doi.org/10.1111/nph.19537>.
- 1171 74 Kothari, S., Beauchamp-Rioux, R., Blanchard, F., Crofts, A.L., Girard, A.,  
1172 Guilbeault-Mayers, X., Hacker, P.W., Pardo, J., Schweiger, A.K., Demers-  
1173 Thibeault, S., Bruneau, A., Coops, N.C., Kalacska, M., Vellend, M. and Laliberté,  
1174 E. (2023) Predicting Leaf Traits across Functional Groups Using Reflectance  
1175 Spectroscopy. *New Phytologist*, **238**, 549–566. <https://doi.org/10.1111/nph.18713>.
- 1176 75 Guo, X., Liu, W., Yang, Y., Liu, G., Ming, B., Xie, R., Wang, K., Li, S. and Hou,  
1177 P. (2023) Matching Light and Nitrogen Distributions in the Maize Canopy to  
1178 Achieve High Yield and High Radiation Use Efficiency. *Journal of Integrative  
1179 Agriculture*, S2095311923004720. <https://doi.org/10.1016/j.jia.2023.12.025>.

1181